Grand-scale Atmospheric Imaging Apparatus (GAIA) and Wind LiDAR Multi-scale Measurements in the Atmospheric Surface Layer

Giacomo Valerio Iungo,[a] Michele Guala,[b,c] Jiarong Hong,[b,d] Nathaniel Bristow,[b,d] Matteo Puccioni,[a] Peter Hartford,[b,d] Roozbeh Ehsani,[b,c] Stefano Letizia,[a] Jiaqi Li,[b,d] and Coleman Moss[a]

[a] *Wind Fluids and Experiments (WindFluX) Laboratory, Department of Mechanical Engineering, The University of Texas at Dallas, Richardson, TX, 75080*

[b] *St. Anthony Falls Laboratory, University of Minnesota, Minneapolis, MN, 55414*

[c] *Department of Civil, Environmental, and Geo-Engineering, University of Minnesota, Minneapolis, MN, 55414*

[d] *Department of Mechanical Engineering, University of Minnesota, Minneapolis, MN, 55414*

Corresponding author: Giacomo Valerio Iungo, valerio.iungo@utdallas.edu

Stefano Letizia’s current afiliation: National Renewable Energy Laboratory, Golden, Colorado

ABSTRACT: Understanding the organization and dynamics of turbulence structures in the atmospheric surface layer (ASL) is important for fundamental and applied research in different fields, including weather prediction, snow settling, particle and pollutant transport, and wind energy. The main challenges associated with probing and modeling turbulence in the ASL are: i) the broad range of turbulent scales associated with the different eddies present in high Reynolds-number boundary layers ranging from the viscous scale (O(mm)) up to large energy-containing structures (O(km)); ii) the non-stationarity of the wind conditions and the variability associated with the daily cycle of the atmospheric stability; iii) the interactions among eddies of different sizes populating different layers of the ASL, which contribute to momentum, energy, and scalar turbulent fluxes. Creative and innovative measurement techniques are required to probe near-surface turbulence by generating spatio-temporally-resolved data in the proximity of the ground and, at the same time, covering the entire ASL height with large enough streamwise extent to characterize the dynamics of larger eddies evolving aloft. To this aim, the U.S. National Science Foundation sponsored the development of the Grand-scale Atmospheric Imaging Apparatus (GAIA) enabling super-large snow particle image velocimetry (SLPIV) in the near-surface region of the ASL. This inaugural version of GAIA provides a comprehensive measuring system by coupling SLPIV and two scanning Doppler LiDARs to probe the ASL at an unprecedented resolution. A field campaign performed in 2021–2022 and its preliminary results are presented herein elucidating new research opportunities enabled by the GAIA measuring system.

CAPSULE: Coupling snow-particle imaging and wind LiDARs for velocity measurements in the atmospheric surface layer can unveil the organization of turbulence structures and offer guidance for improved wall models needed for accurate numerical simulations.

1. Introduction

Understanding the physical mechanisms underpinning the organization and dynamics of turbulent coherent structures in the atmospheric surface layer (ASL) is important for several scientific and engineering areas, such as weather prediction modeling (Muñoz-Esparza et al. 2014; Jiménez et al. 2012; Juliano et al. 2022), snow settling and drift (Brun et al. 1989; Bartelt and Lehning 2002; Bristow et al. 2023), pollen and pollution transport (Sofiev et al. 2006; Chamecki et al. 2009), wind energy (Önder and Meyers 2018; Veers et al. 2022), urban flows (Lane et al. 2013; Lamer et al. 2022), low-level wind shear, and urban meteorology (Liu et al. 2019b). The ASL is the region at the bottom of the atmospheric boundary layer, with a typical thickness of O(10^2 m), where turbulent fluxes and stresses vary by less than 10% of their magnitude (Stull 1988). The classical description of a turbulent boundary layer includes a background mean flow perturbed by flow fluctuations induced by coherent turbulent structures, or “eddies”, which are organized as a cascade of momentum-exchanging structures draining kinetic energy from the mean flow (Stull 1988; Pope 2000; Jiménez 2012; Cardesa et al. 2017).

Eddies of different sizes populating a turbulent boundary layer are generated through different physical processes and evolve over different regions leading to specific statistical and spectral footprints in the flow. In particular, the high-frequency range of a turbulent boundary layer is dominated by small-scale eddies, whose energetic characteristics reflect into the Kolmogorov $k_x^{-5/3}$ inertial sub-range of the streamwise velocity energy spectrum (where k_x is the streamwise wavenumber) (Perry et al. 1986; Mahrt 1989; Marusic et al. 1997).

Moving toward lower frequencies, the logarithmic layer can be pictured as a forest of randomly-distributed geometrically-similar eddies generated from the ground, whose streamwise dimension is proportional to their distance from the wall, and for this reason, they are dubbed “wall-attached eddies” (Perry and Marušić 1995; Hwang and Sung 2018; Hu et al. 2020; Puccioni et al. 2023a). Different statistical and spectral properties of wall-attached eddies can be predicted through a linear super-position of their elementary contributions, which is the core assumption of Townsend's attached-eddy hypothesis (Townsend 1976).

The motion induced by turbulent eddies can be characterized by the turbulent kinetic energy (TKE), which represents the kinetic energy per unit mass and is calculated as half of the sum of the variances of the velocity fluctuations (Pope 2000), and the Reynolds stresses, which are calculated from the cross-correlation between different turbulent velocity fluctuations. In a turbulent boundary layer, more than 50% of the TKE and Reynolds stresses is carried by eddies with streamwise wavelength larger than the boundary layer height (Ganapathisubramani et al. 2005; Hutchins and Marusic 2007a; Puccioni et al. 2023a). These large eddies, which are denoted, e.g., as "very-large-scale motions" (VLSMs) or superstructures (Kim and Adrian 1999; Guala et al. 2006; Balakumar and Adrian 2007; Hutchins and Marusic 2007a), have a morphology and energy content not directly affected by the ground, hence they are classified as wall-detached eddies (Högström 1990, 1992; Högström et al. 2002; Baars and Marusic 2020; Hu et al. 2020). The turbulence research community has not achieved yet a consensus on the genesis of these large coherent structures, yet the most accredited theories associate their generation either with the streamwise concatenation of wall-attached eddies, top-down entrainment of turbulent bulges within the boundary layer, or specific instability mechanisms (Guala et al. 2006; Balakumar and Adrian 2007). The main signature of VLSMs and superstructures consists in the presence of a sharp energy peak in the low-frequency turbulence range of the streamwise velocity energy spectra (Kim and Adrian 1999; Guala et al. 2006, 2011), while their size should scale with the boundary layer height, and, thus, it can also be affected by atmospheric thermal stability (Mouri et al. 2019; Krug et al. 2019).

All the above-mentioned turbulent structures with their different genesis, morphology, and energy content interact through different processes throughout the boundary layer. For instance, several laboratory experiments and numerical simulations have shown how VLSMs can modulate near-surface turbulence both in terms of energy content and characteristic wavelengths (Mathis et al. 2009; Talluru et al. 2014; Liu et al. 2019a; Lee and Moser 2019; Salesky and Anderson 2020). Further, the spatio-temporal organization of the various turbulent eddies determines the intensity of the local shear, which is typically associated with the presence of flow regions with roughly constant velocity, therefore termed "Uniform Momentum Zones" (UMZs) (Meinhart and Adrian

1995; de Silva et al. 2016; Laskari et al. 2018; Heisel et al. 2020), delimited by layers of intense shear layers typically populated by aligned vortices.

One of the most suitable non-dimensional parameters to characterize the size range of turbulent eddies populating a boundary layer is the friction Reynolds number, $Re_\tau = u_\tau \delta/\nu$, which quantifies the ratio between the largest turbulent coherent motions (proportional to the outer-scale boundary layer height, δ), and the smallest eddies with scales proportional to ν/u_τ, where ν is the kinematic viscosity and u_τ is the friction velocity. Therefore, increasing Re_τ is equivalent to increasing the spectral range between the large energy-containing turbulent structures, e.g. VLSMs and superstructures, and small-scale eddies.

Investigating boundary layers with a high Reynolds number is instrumental to achieving a deeper understanding of the physical processes governing turbulence; to this aim, dedicated high Reynolds-number laboratory-scale facilities (Marusic et al. 2010; Smits et al. 2011; Marusic and Monty 2018) and numerical tools (Jiménez 2004; Jiménez and Moser 2007; Lee and Moser 2015, 2019) have been developed. For the same reason, the ASL can provide unique opportunities to perform high Reynolds-number boundary-layer turbulence research being that the ASL is one of the turbulent boundary layers with the largest friction Reynolds number achieved terrestrially O(10^6) (Kunkel 2003; Kunkel and Marusic 2006; Metzger et al. 2007; Marusic and Hutchins 2008; Guala et al. 2011; Heisel et al. 2018; Huang et al. 2021; Puccioni et al. 2023a), where large energy-containing coherent structures can achieve wavelengths of the order of O(km), while dissipative turbulent processes occur at scales of the order of O(mm) (Pope 2000; Jiménez 2012; Cardesa et al. 2017).

Investigations of ASL turbulence require measurement techniques providing suficient spatio-temporal resolution near the ground to probe near-surface turbulence. At the same time, the measurement domain should attain locations close to the ASL height to monitor the evolution of larger turbulent structures and their interactions with the near-surface turbulence. To this aim, early particle image velocimetry (PIV) experiments in the ASL were performed using smoke generators or similar tracers over observational domains extending about 1–3 m above the ground (Hommema 2003; Morris et al. 2007). The challenges in seeding the flow roughly uniformly over larger regions inspired the adoption of natural tracers, such as highly-reflective snow particles, which then led to the development of the Super-Large PIV (SLPIV) (Hong et al. 2014; Toloui et al. 2014). The ability of SLPIV to probe the wind velocity variability with high spatial resolution (O$(10^{-1}\,\mathrm{m})$)

over large domains attaining heights of about 20 m (Toloui et al. 2014) was leveraged to investigate ASL turbulent structures (Heisel et al. 2018), wakes generated from a utility-scale wind turbine (Dasari et al. 2019), and the effects of wind turbine wakes on surface turbulent fluxes (Abraham and Hong 2021).

While SLPIV provides adequate spatio-temporal resolution to probe near-surface turbulence, the limited vertical extent in such a configuration (≈ 20 m) does not enable to directly monitor interactions of near-surface turbulence with larger coherent structures evolving aloft (Hu et al. 2020; Puccioni et al. 2023a). For the Grand-scale Atmospheric Imaging Apparatus (GAIA) field campaign, this has been the motivation to couple SLPIV measurements with velocity measurements performed with wind light detection and ranging (LiDAR). Over the last few decades, LiDAR has become a compelling remote sensing technique to investigate atmospheric turbulence and flows evolving in the atmospheric boundary layer. For instance, LiDAR scans can be optimally designed to probe the atmospheric boundary layer and wakes generated by utility-scale wind turbines (Iungo and Porté-Agel 2013, 2014; Fuertes et al. 2014; Iungo 2016; Letizia et al. 2021a; El-Asha et al. 2017; Zhan et al. 2020; Letizia et al. 2021b; Iungo et al. 2022, e.g). LiDAR measurements were performed to detect the inverse-power law spectral region (Calaf et al. 2013; Puccioni et al. 2023a) and the inertial sub-layer (Iungo et al. 2013) from the streamwise velocity energy spectra measured within the ASL.

The GAIA project aims to develop, deploy, and evaluate a pioneering experimental apparatus capable of probing atmospheric turbulence and particle transport using an imaging-based approach. This system has the potential to capture highly dynamic phenomena in the atmosphere at an unprecedented level of spatio-temporal resolution. The initial version of GAIA integrates SLPIV, which utilizes snow-particle imaging, with scanning Doppler LiDARs to facilitate accurate spatio-temporal measurements of near-surface turbulence, larger turbulent eddies at higher altitudes, and their interplay via different turbulent processes, including amplitude-frequency modulations (Mathis et al. 2009; Talluru et al. 2014; Liu et al. 2019a; Salesky and Anderson 2020).

In this manuscript, the experimental apparatus is described together with the results obtained from the first field campaign performed in winter 2021-2022. Technical details of the various instruments used for the GAIA field campaign and an overview of the measurement strategy are provided in Sect. 2. Samples of the data sets collected with SLPIV are reported in Sect. 3, while the LiDAR measuring strategy and an overview of the data sets collected are detailed in Sect. 4. Results from the joint SLPIV-LiDAR statistical analysis are provided in Sect. 5, and concluding remarks are reported in Sect. 6. Finally, more details on the post-processing of the SLPIV data are provided in Appendix A.

2. The GAIA field campaign

The SLPIV apparatus was deployed at the University of Minnesota Eolos Wind Energy Research Field Station in Rosemount (Hong et al. 2014; Nemes et al. 2017; Heisel et al. 2018; Dasari et al. 2019; Abraham and Hong 2021), concurrently with the mobile LiDAR station developed at the University of Texas at Dallas (UTD) (El-Asha et al. 2017; Zhan et al. 2020; Letizia et al. 2021a,b; Puccioni et al. 2023a) over the period between December 5, 2021, and February 24, 2022, to perform four deployments at various locations, which are indicated in Fig. 1 and reported in Table ES1 of the supplemental material. Selected photos from the various deployments are reported in Fig. 2, while a schematic view of the simultaneous deployments of SLPIV and the scanning Doppler LiDARs is reported in Fig. 3.

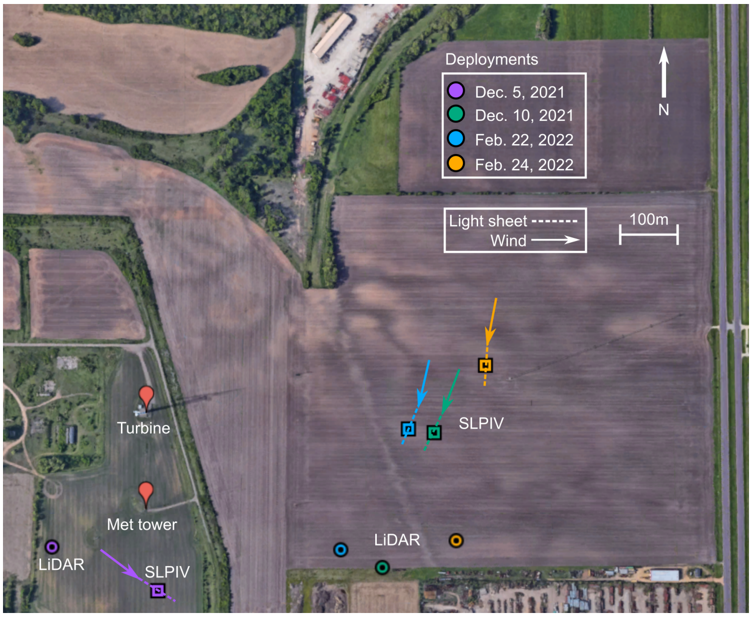

Fig. 1. GAIA field campaign at the Eolos site. Circle markers indicate LiDAR positions, square markers indicate SLPIV light sheet positions and arrows indicate mean wind directions during the deployments. Credits: Google Earth.

Fig. 2. Photos of the GAIA field campaign: (a) SLPIV light sheet pointing vertically; (b) SLPIV light sheet pointing horizontally; (c) deployment of the scanning Doppler LiDARs.

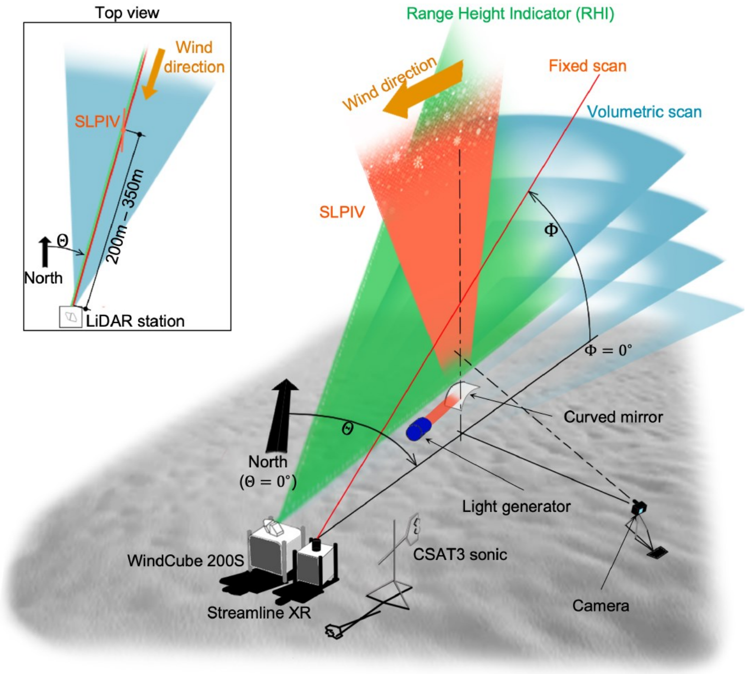

Fig. 3. Schematic of the simultaneous deployment of the UTD mobile LiDAR station and SLPIV (figure not to scale). The inset on the top left corner reports the top view of the experimental setup.

The SLPIV equipment consists of a trailer-mounted illumination system and cameras. A nearly 100 m tall light sheet is generated using a 5 kW searchlight focused on a ⍰ 0.3 m thick beam, which is then spread with a curved mirror to generate a light sheet pointing either vertically or horizontally (Fig. 2a and 2b, respectively). Images of the illuminated snow particles are captured with different cameras, such as a Nikon D610, Sony α7Rii, and α7Siii (camera specifications are outlined in Table ES2 of the supplemental material).

The spatial resolution of the SLPIV is determined by the snow particle response time and, thus, by their inertial properties, e.g. snow crystal size and density. In other words, the characteristics of the snow particles determine whether snow is a good inertial flow tracer for the SLPIV (Eaton and Fessler 1994). Encouraging results were previously documented for similar SLPIV deployments (Hong et al. 2014; Toloui et al. 2014; Heisel et al. 2018), for which the Stokes number (i.e. the ratio between the particle response time and the flow timescale) was estimated to be ≈ 0.1 for flow spatial scales of the order $O(10^{-1}\ m)$, which indicates a good inertial behavior of the snow particles.

Coupled with the SLPIV setup, the UTD mobile LiDAR station was deployed to probe a measurement volume including the SLPIV field of view. This setup encompasses two coordinated scanning Doppler LiDARs (Fig. 2c), i.e. a Streamline XR manufactured by Halo Photonics and a Windcube 200S manufactured by Leosphere, a surface-flux station, and an infrastructure for remote control, scan setup, and data transfer for the instruments deployed. Technical details of each LiDAR are reported in Table ES3 of the supplemental material. The surface-flux station encompasses one CSAT3 sonic anemometer manufactured by Campbell Scientific Inc. installed within a few meters from the LiDARs at a 2 m height.

For each deployment, a Cartesian reference frame (x, y, z), is selected along streamwise, spanwise, and vertical directions, respectively. The corresponding mean velocity field is indicated as (U, V, W), while the respective zero-mean fluctuating velocity components are (u', v', w'), and t is time.

3. SLPIV test case: Probing near-surface turbulence in the ASL

Two-velocity-component vector fields can be retrieved from the continuously-recorded images captured by SLPIV over a vertical plane roughly aligned with the mean wind direction (see Appendix A for more details on the post-processing of SLPIV data). A misalignment of the SLPIV light sheet with the wind direction can lead to underestimation of the streamwise velocity component because the cross-plane velocity component is not probed from the SLPIV system. However, considering that the light sheet has a cross-width between 30 cm and 50 cm, then a wind-direction misalignment with the orientation of the light-sheet plane up to 30° can be handled with negligible effects on the measured streamwise velocity considering a sampling rate of 30 frames per second and a wind speed smaller than 5 m s^{-1}. The dimensions of the field of view and spatio-temporal resolution of the SLPIV are adjusted depending on the specific objectives of the experiments. For instance, to investigate near-surface turbulence, the SLPIV field of view has a larger dimension along the streamwise direction, while to investigate interactions of near-surface turbulence with larger turbulent structures evolving aloft, the SLPIV domain is extended mainly in the vertical direction.

For this section, we selected data collected during the deployment performed on February 22, 2022. Highly spatially-resolved images were acquired focusing on a $\sim$ 10 m × 10 m field of view, at a 120 Hz frame rate, and for a 15-minute recording time. These measurements enable probing wind-velocity variability for scales ranging from the Taylor microscale, which is the largest eddy size for which viscous effects are still important ($\lambda_T \approx$ 0.1 m, see Heisel et al. (2018) under similar ASL conditions), up to the size of large energy-containing coherent structures evolving within the logarithmic region (Adrian et al. 2000b; Monty et al. 2009; Heisel et al. 2018). The key signature of these turbulent coherent structures is the presence of vortices aligned along internal shear layers (Christensen and Adrian 2001; Heisel et al. 2021) delimiting zones with nearly uniform velocity (UMZs) (Meinhart and Adrian 1995; Laskari et al. 2018; Heisel et al. 2020).

The following showcases a sample of the high-resolution spatio-temporal flow characterizations that can be attained using SLPIV. Fig. 4a shows the streamwise velocity averaged at each time along the streamwise extent of the SLPIV field of view and reported as a function of time and height, z. If we analyze only a sub-period of this velocity map, as reported in Fig. 4b, we can identify an inclined pattern in the flow roughly demarcating the boundary between two regions with significantly different velocities (UMZs), namely lower streamwise velocity below (predominantly red color) and higher streamwise velocity above (predominantly blue color). This flow feature is consistent with the signature of hairpin packets or ramp-like structures separating two adjacent UMZs, as conjectured through previous wind tunnel and field experiments (Adrian et al. 2000b, e.g.), and may be considered as an archetypal realization of turbulent structures generated at the surface.

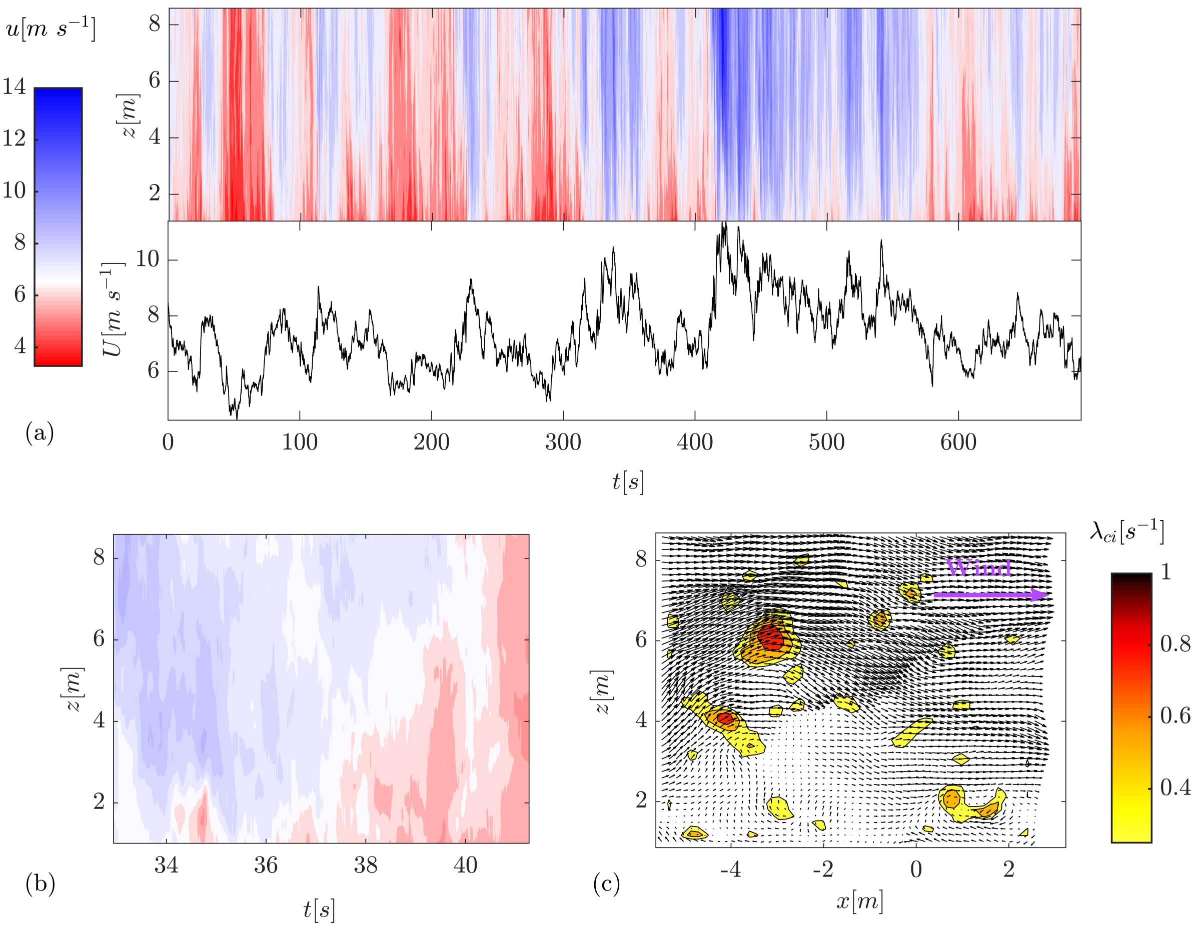

Fig. 4. SLPIV measurements collected on February 22, 2022: (a) colormap of the streamwise velocity averaged along the streamwise extent of the SLPIV field of view and reported as a function of time. In the lower panel, the corresponding vertically-averaged velocity is reported; (b) magnified region from (a) over a sub-period; (c) vortex identification through the λ_{ci} criterion for a SLPIV snapshot corresponding to $t = 32$ s (flow direction is left-to-right).

Upon analyzing the SLPIV snapshot for a generic time from the velocity fields illustrated in Fig. 4a or Fig. 4b, groups of vortices can be observed. The vortex cores are identified through the swirling strength parameter, λ_{ci} (see Fig. 4c), which allows marking local swirling motion based on the complex eigenvalues of the velocity-gradient tensor (Jeong and Hussain 1995). In turbulent boundary layers, these vortices are observed to be statistically arranged near shear layers evolving from the ground, inclined at a forward $10^\circ - 15^\circ$ angle (Adrian et al. 2000b; Ganapathisubramani et al. 2005; Heisel et al. 2018).

The characterization of the morphology, location, and dynamics of these eddies is instrumental in providing a physical interpretation of the turbulent statistics, such as Reynolds stresses, TKE, and dissipation rate (Albertson et al. 1997; Christensen and Adrian 2001). While these turbulent quantities can be quantified from measurements collected through classical anemometers installed on meteorological towers (Bodini et al. 2020), and more recently also through Doppler LiDARs (Sanchez Gomez et al. 2021), interpreting the dynamic role of vortex organization on the spatio-temporal evolution of turbulence can be very challenging.

The analysis of the SLPIV snapshots and velocity time series can also provide information on the effects induced by larger structures that may evolve aloft, yet leave a profound signature on the turbulence statistics closer to the ground (Hutchins and Marusic 2007b; Mathis et al. 2009; Guala et al. 2010). Fig. 4a displays low-frequency velocity fluctuations that are easily discernible even through visual inspection, as evidenced by the vertically-averaged velocity signal depicted in the lower panel of the figure (with typical periods around 150 s). These low-frequency velocity fluctuations can be induced by structures having streamwise wavelengths comparable, or even larger, than the ASL height (Hutchins and Marusic 2007b; Mathis et al. 2009). These large structures cannot be directly probed through SLPIV in the current near-surface configuration, because typically evolve over heights larger than that attained with the SLPIV field of view (Puccioni et al. 2023a). Therefore, it is crucial to couple SLPIV and scanning Doppler LiDAR measurements to accurately resolve the flow over larger volumes reaching the ASL top.

4. LiDAR scanning strategy

As detailed in Sect. 2, two pulsed scanning Doppler LiDARs were deployed during the GAIA field campaign at locations selected to have the direction connecting the LiDAR position with the center of the SLPIV field of view roughly aligned with the mean wind direction (Fig. 1). This setup would ensure that the LiDAR radial velocity is practically insensitive to the mean transverse velocity component. Geometric details of the LiDAR scans for each deployment are reported in Table ES4 of the supplemental material.

The Halo Streamline XR LiDAR was devoted to performing fixed-point measurements by locating a gate roughly at the middle point of the horizontal extent of the SLPIV field of view and a height of about 30 m above the ground. The horizontal distance between the LiDARs and the SLPIV field of view was selected to ensure a low elevation angle of the LiDAR laser beam (between 1.7° and 6.8° for this experiment) to maximize LiDAR sensitivity to the streamwise velocity component. The LiDAR fixed-point measurements were performed using a range gate of 18 m, sampling frequency of 2 Hz, and sampling duration between 20 and 60 minutes.

The radial wind speed, $\square_{\square}$, measured by a Doppler LiDAR represents the projection of the wind velocity vector along the line-of-sight of the LiDAR laser beam (Cheynet et al. 2017; Zhan et al. 2020; Puccioni and Iungo 2021):

$$\square_{\square}(\square,\square) = \square(\square,\square)\cos(\square-\square_{\square})\cos\square + \square(\square,\square)\sin(\square-\square_{\square})\cos\square + \square(\square,\square)\sin\square, \qquad (1)$$

where $\square$ and $\square$ are the azimuth and elevation angles of the LiDAR laser beam, respectively, $\square_{\square}$ is the wind direction estimated from the LiDAR or the sonic-anemometer data, $\square$ is time, and $(\square,\square,\square)$ are the streamwise, spanwise, and vertical velocity components, respectively. Therefore, considering the low elevation angle used for the LiDAR fixed-point measurements ($\square < 6.8^{\circ}$) and the LiDAR azimuth angle set equal to the mean wind direction, then the wind streamwise velocity can be estimated as:

$$\square(\square,\square,\square,\square) \approx \frac{\square_{\square}(\square,\square,\square)}{\cos(\square-\square_{\square})\cos\square}. \qquad (2)$$

For more details on the post-processing of the LiDAR data, the reader is referred to Puccioni et al. (2023a). As typically performed with the UTD mobile LiDAR station (Puccioni et al. 2023b), simultaneously to the high-sampling-frequency fixed-point measurements, which are mainly devoted to probe wind turbulence at different heights, the other scanning LiDAR, i.e. a Windcube 200S, performed a composite of scans with a lower temporal resolution, namely vertical azimuth display (VAD) scans to characterize the vertical profile of mean wind velocity and direction over the site, range height indicator (RHI) scans over the SLPIV plane with the aim at probing large-scale flow variability, and volumetric scans roughly centered at the SLPIV position to characterize the spatial heterogeneity of the wind field over the site. It is worth noting that the scanning parameters of the RHI and volumetric scans, i.e. angular resolutions, azimuth and elevation limits, and scanning speed, are optimally selected through the LiDAR Statistical Barnes Objective Analysis (LiSBOA) procedure (Letizia et al. 2021a) as a trade-off among the size of the scanning area/volume, spatio-temporal resolution, and accuracy of the retrieved statistics.

LiDAR data collected through fixed-point measurements and VAD scans will be analyzed in detail in the next section. Here, as an example, we show in Fig. 5a and Fig. 5b mean and variance, respectively, of the streamwise velocity retrieved from the RHI scans collected on February 22, 2022. The SLPIV measurement area is approximately 240 m away from the LiDAR location, measuring about 20 m in width and 10 m in height. Therefore, it is evident that the velocity field surrounding the SLPIV field of view experiences significant large-scale variability in both vertical and streamwise directions. This spatial heterogeneity is even more evident for the streamwise-velocity variance (Fig. 5b), which suggests that significant large-scale turbulent dynamics might be observed, as will be discussed in the following section.

Finally, the mean and variance of the streamwise velocity obtained from the volumetric scans performed on the same day of February 22, 2022, are retrieved over a 3D structured Cartesian grid through the LiSBOA procedure (Letizia et al. 2021a,b) (Fig. 5c and Fig. 5d, respectively. It is noteworthy that a certain level of heterogeneity in the flow is observed in all three Cartesian directions from the volumetric scans. This spatial information gathered through the LiDAR data

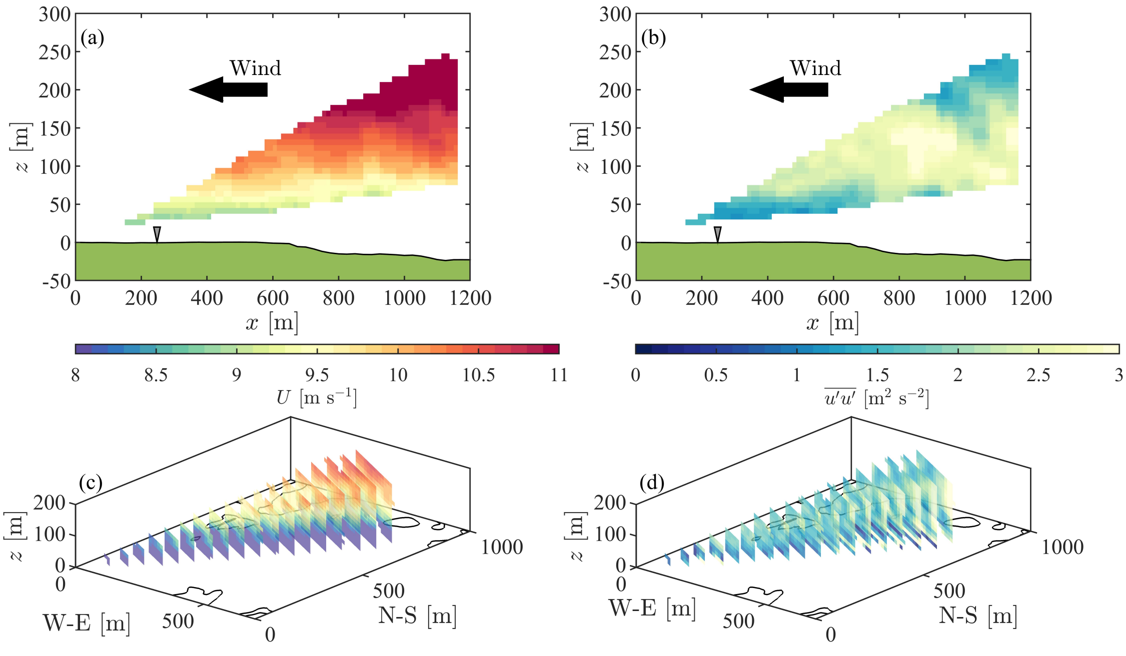

Fig. 5. Overview of the LiDAR measurements performed on February 22, 2022: Mean streamwise velocity retrieved from the RHI scans (a) and volumetric scans (c); Streamwise velocity variance retrieved from the RHI scans (b) and the volumetric scans (d). In (a) and (b), the SLPIV field of view is reported with a grey triangle.

will be instrumental to analyze and interpret the SLPIV measurements and identify interactions between VLSMs, wall-attached eddies, and near-surface turbulence.

5. Integration of SLPIV and wind LiDAR measurements

a. Vertical profiles of the velocity statistics and single-point simultaneous measurements

In this section, we provide an overview of the multiscale flow characterization that can be performed throughout the ASL with the composite vertical profiles of the mean velocity and Reynolds stresses obtained through simultaneous measurements performed with the SLPIV, scanning Doppler LiDARs, and a sonic anemometer. For this analysis, we consider data collected on December 11, 2021, at 2:00 AM UTC for a duration of 22 minutes. The local atmospheric stability is characterized through the Obukhov length (Monin and Obukhov 1954), which is calculated from the sonic-anemometer data as $L = -u_*^3 T/(\kappa g \overline{w'\theta'})$, where $\kappa = 0.41$ is the von Kármán constant, g is the gravity acceleration, $\overline{w'\theta'}$ is the vertical heat flux and T is the mean temperature, which is equal to 271.5 K for the selected data set. The resulting Obukhov length is $L = 839$ m, which corresponds to a stability parameter of $z/L \approx 0.002$ suggesting that for the selected data set turbulence is essentially driven by mechanical shear with minimal effects associated with thermal stratification (Stull 1988; Wyngaard et al. 1998; Metzger et al. 2007).

In Fig. 6a, the vertical profile of the time-averaged streamwise velocity is fitted with the logarithmic law of the wall for a neutrally-stratified boundary layer (Clauser 1954; Stull 1988): $U = u_*/\kappa \cdot \log(z/z_0)$ and reported with a black line. The fitting procedure provides a friction velocity of $u_* = 0.328 \pm 0.015$ m s^{-1}, and an aerodynamic roughness length of $z_0 = 1.18 \pm 0.49$ mm, which are estimated with an R-square value of 0.971 with a 95% confidence level. The value obtained for z_0 is in good agreement with previous estimates obtained for boundary layers evolving on fresh snow over flat terrains (Gromke et al. 2011).

The availability of the sonic-anemometer data collected at 2-m height enables a further estimate of the friction velocity through the eddy-covariance method (Stull 1988): $u_* = \left(\overline{u'w'}^2 + \overline{v'w'}^2\right)^{0.25}$. This alternative approach provides a friction velocity of 0.32 m s^{-1}, which agrees well with the value obtained from the composite velocity profile of Fig. 6a.

The composite vertical profile of the time-averaged streamwise velocity shows a generally good agreement among the statistics obtained from different instruments, in particular between the sonic

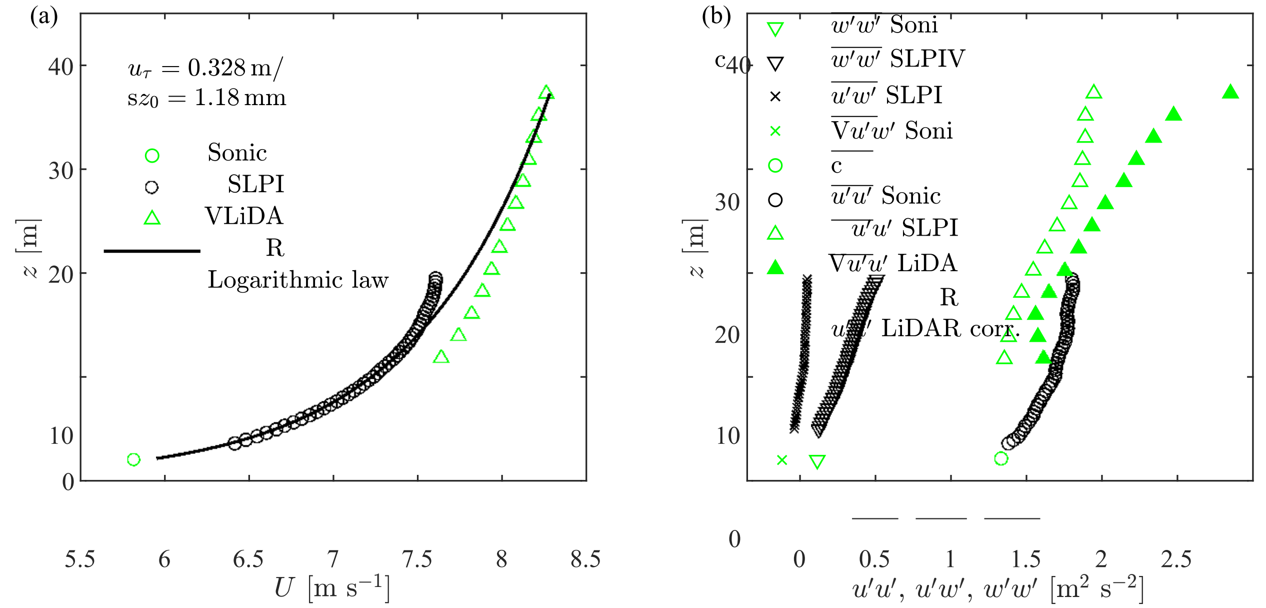

Fig. 6. Vertical profiles of the statistics obtained from simultaneous measurements performed with SLPIV, sonic anemometer, and LiDAR fixed-point measurements on December 11, 2021, 2:00 AM - 2:22 AM UTC: (a) mean streamwise velocity; (b) Reynolds stresses.

anemometer at 2-m height and the SLPIV (Fig. 6a). A slight deviation is observed for the LiDAR data for which larger velocities than those measured by the SLPIV are observed for overlapping heights. Besides accuracy in the velocity measurements performed with SLPIV and the LiDAR fixed-point measurements, this discrepancy (< 0.3 m s^{-1}) can also be ascribed to the averaging of the SLPIV data along the streamwise direction, the different physical locations sampled from the two instruments, and to the site-specific flow heterogeneity already singled-out through the RHI and volumetric LiDAR scans (Fig. 5).

For the same data set under investigation, the composite vertical profiles of the Reynolds stresses are reported in Fig. 6b. A very good agreement is observed for the Reynolds stress, the stream-wise and vertical velocity variance measured through the SLPIV and the sonic anemometer. As expected, the streamwise velocity variance calculated from the LiDAR fixed-point measurements is underestimated compared to SLPIV statistics calculated over their overlapping vertical range. This feature is due to the spatial averaging associated with the LiDAR measuring process over each probe volume (see, e.g., Frehlich et al. 1998; Brugger et al. 2016). A better agreement between the SLPIV and LIDAR streamwise variance is achieved by applying the correction method proposed by Puccioni and Iungo (2021) (green-filled symbols in Fig. 6b). The Reynolds-stress $\overline{\square'\square'}$ values obtained with SLPIV near the surface are reasonably close to the respective sonic-anemometer velocity statistics. With increasing heights, SLPIV tends to underestimate the Reynolds shear stress $\overline{⍰'⍰'}$, while overestimating the vertical velocity variance. This may be an effect due to the combination of relatively low spatial resolution of the SLPIV measurements with a background large-scale unsteadiness of the flow.

The inter-comparison of the streamwise velocity measured with the different instruments is now performed in the temporal domain. For this analysis, we consider data collected through the sonic anemometer at 2-m height and SLPIV at 3.5-m height. Further, we perform the inter-comparison of the data collected simultaneously through the LiDAR fixed-point measurements and SLPIV at four overlapping heights (12 m, 14 m, 16 m, and 18 m).

To compare in time the streamwise velocity signals collected with the different instruments, we should take into account a time lag, ⍰, associated with the advection of turbulent structures over the streamwise distance, Δ⍰, separating instruments deployed at different locations. For each set of velocity measurements collected with two different instruments, the time lag ⍰ is estimated through the cross-correlation function calculated between the corresponding time series (Han et al. 2019).

The cross-correlation analysis is first performed for the streamwise velocity measured by the sonic anemometer at 2 m height and the SLPIV at 3.5 m height, then averaged over the streamwise extent of the SLPIV field of view. The time lag between these two time series is estimated as ⍰ ≈ 35 s, corresponding to an advection velocity of about 7 m s^{-1}. This estimated advection velocity is slightly larger than the mean velocity measured through the vertical profile reported in Fig. 6a. Similar discrepancies between estimated advection velocity and measured local mean velocity were already observed from previous experiments (Erm and Joubert 1991; Dennis and Nickels 2008; LeHew et al. 2011).

A similar analysis performed for the LiDAR fixed-point measurements and SLPIV data collected for the overlapping heights produces estimates of ⍰ between 11.5 s and 18 s, corresponding to advection velocities between 8.3 m s^{-1} and 9.1 m s^{-1}, again slightly larger than the time-averaged streamwise velocity at the same heights. After being re-aligned in time, the velocity signals demonstrate a high degree of agreement, as evidenced by the qualitative comparison presented in Fig. 7a between the sonic anemometer and SLPIV data. Similar results are obtained when

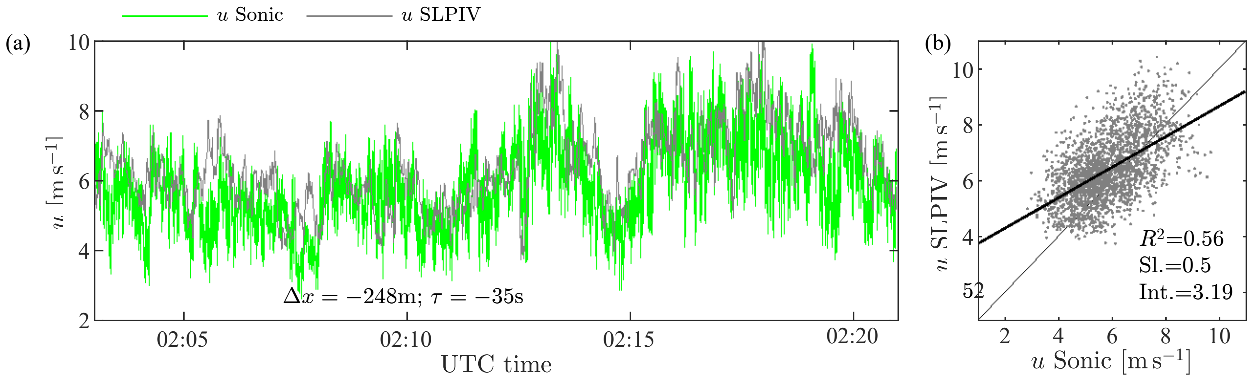

Fig. 7. Single-point analysis of streamwise velocity collected with the sonic anemometer and the SLPIV on December 11, 2021: (a) Portion of the time series; (b) Linear regression.

comparing the re-aligned velocity signals from SLPIV and the LiDAR fixed-point measurements for the overlapping heights of 12 m, 14 m, 16 m, and 18 m, (Figs. 8a, c, e, g, respectively).

These results are further corroborated by carrying out a linear regression analysis between the re-aligned streamwise velocity signals collected by the various instruments at the same height. The linear regression between the sonic anemometer and SLPIV data leads to a correlation value that is not very high ($R^2 = 0.56$, see Fig. 7b). This feature is likely associated with the 248-m separation distance between the two instruments, slightly different heights (2 m for the sonic anemometer and 3.5 m for SLPIV) and, more importantly, the relatively high spatio-temporal resolutions of both instruments capturing flow distortions of small-scale turbulent structures advected over a relatively large distance.

The linear regression analysis between SLPIV and LiDAR data is shown in Figs. 8b, 8d, 8f, 8h for the different heights. The correlations are generally good and improved with respect to the linear regression between SLPIV and sonic anemometer (slope larger than 0.71, intercept lower than 2.4 m s^{-1}, and R^2 value larger than 0.81). Such a better correlation, as compared to the SLPIV/sonic anemometer inter-comparison, is achieved thanks to the shorter streamwise distance between the LiDAR gates and the SLPIV domain (< 150 m), and the spatial averaging within the SLPIV field and LiDAR gate, all limiting the space-time deformation of the velocity field.

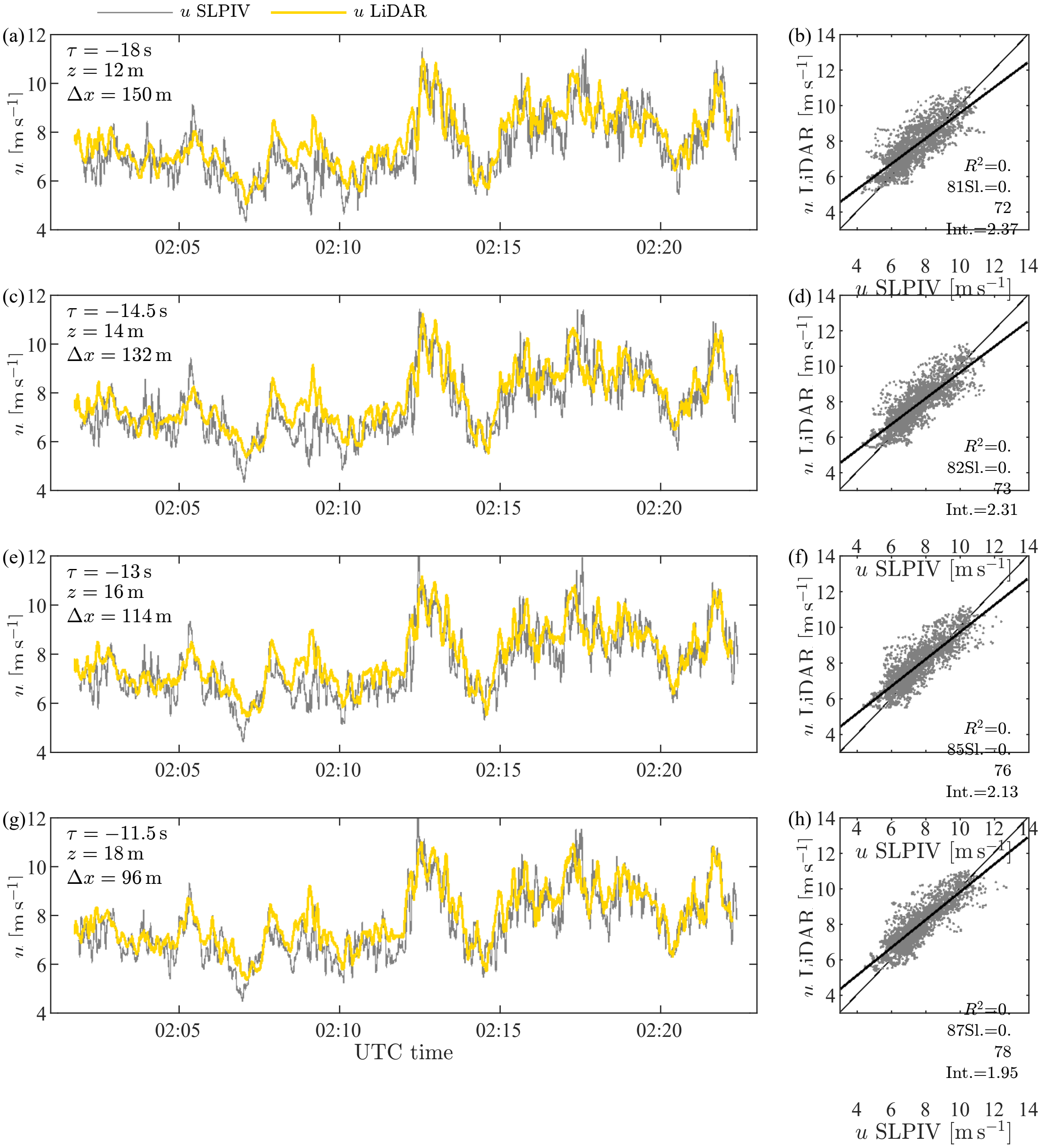

Fig. 8. Single-point analysis of streamwise velocity calculated from the LiDAR fixed-point measurements and SLPIV on December 11, 2021, at heights of 12 m, 14 m, 16 m, and 18 m: (a), (c), (e), (g) Time series; (b), (d), (f), (h) Linear regression.

b. Conditional statistics of SLPIV data based on wind LiDAR measurements

In this section, we provide an initial, quantitative characterization of how large-scale turbulent motions, which the wind LiDARs probed during the GAIA experiment, modulate near-surface

turbulence captured by the SLPIV. Specifically, we describe how the occurrence of high- and low-streamwise-velocity events, which might be induced by VLSMs or superstructures evolving at a certain distance from the ground (Puccioni et al. 2023a), can affect the organization of turbulent eddies populating the near-surface region, and, thus, Reynolds stresses, TKE, and dissipation rate.

From the deployment performed on February 22, 2022, we first identify high- and low-streamwise-velocity events from the velocity time series, [illegible], obtained from the LiDAR fixed-point measurements at a height of 19 m, i.e. slightly above the SLPIV field of view. The selected high- and low-streamwise-velocity events (red and blue markers in Fig. 9a, respectively) are identified from velocity samples with values laying outside of the 25th–75th percentile range estimated for the entire duration of the time series.

The SLPIV snapshots corresponding to the selected high- and low-streamwise-velocity events are then analyzed to characterize the organization of the turbulent eddies in the near-surface region by leveraging the high spatial resolution of SLPIV in probing simultaneously streamwise and vertical velocity components over a plane roughly aligned with the mean wind direction.

As a first step, we classify the streamwise velocity field into Uniform Momentum Zones, UMZs, for the selected low- and high-streamwise-velocity events, as reported in Fig. 9b and 9c, respectively. UMZs are flow regions bounded by internal shear layers, which are deemed to be important flow features for the resulting Reynolds shear stresses and turbulence intensity (Meinhart and Adrian 1995; Laskari et al. 2018; Heisel et al. 2020). UMZs are identified from SLPIV snapshots by local peaks in the histograms of the instantaneous velocity, which are then associated with the respective modal velocities characterizing adjacent UMZs (Heisel et al. 2020). For the low-streamwise-velocity event, the internal shear layers (ISLs) delimiting adjacent UMZs have similar inclinations, namely with increasing heights moving downstream (Fig. 9b). Delving more in-depth to investigate the organization of turbulent eddies in the near-surface region, it is observed that the majority of the vortices with negative swirling strength [illegible] i.e. indicating prograde vortices rotating with the mean shear, in Fig. 9d, are located in the proximity of the ground and confined within a region with an inclination similar to those of the ISLs shown in Fig. 9b. This organization of eddies in the proximity of the ground resembles the signature of hairpin-vortex clusters into a ramp-like coherent structure, or packet, as already shown from previous wind tunnel experiments, direct numerical

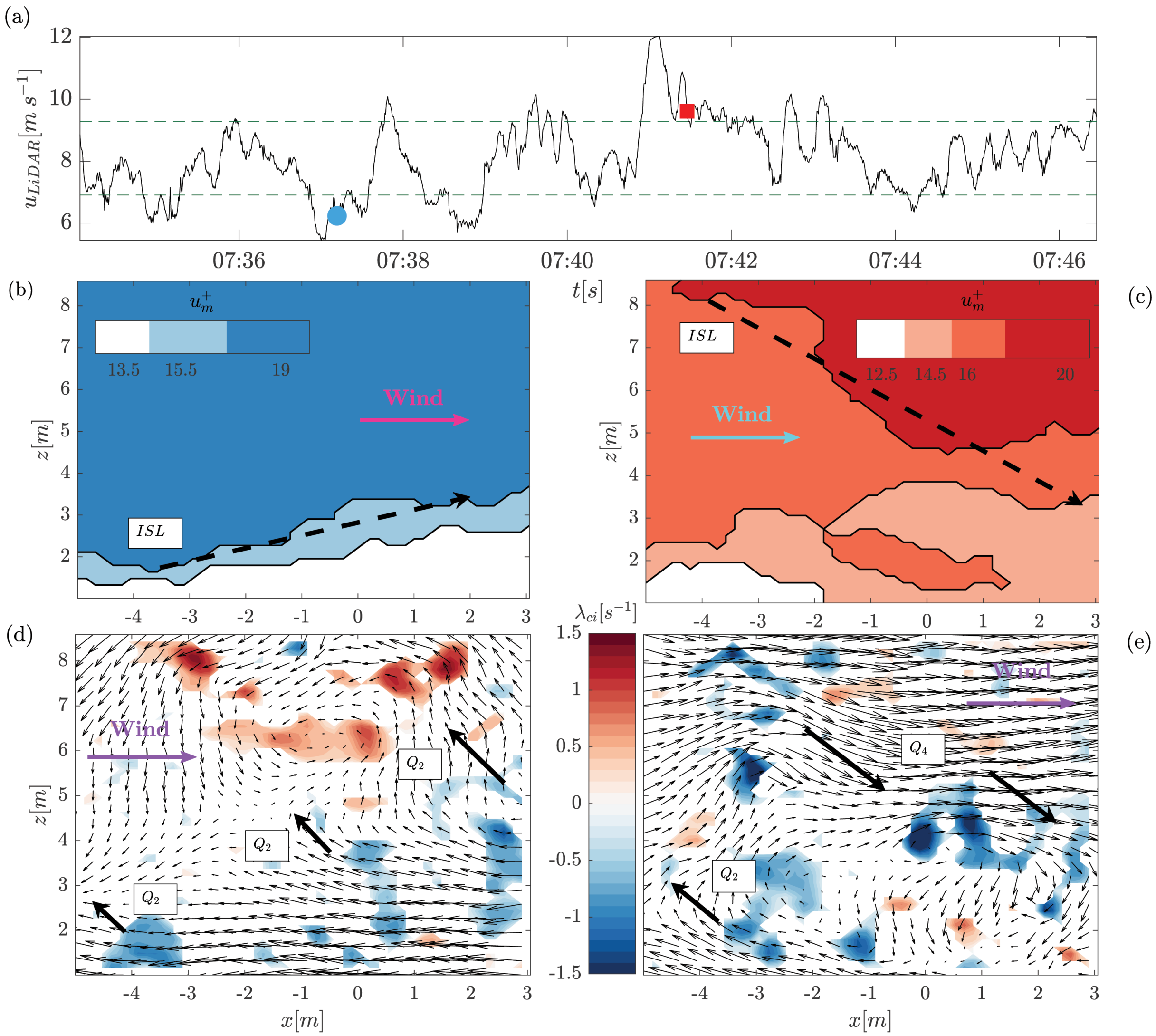

Fig. 9. Conditional sampling of the SLPIV data based on wind LiDAR data: (a) Time-series of the streamwise velocity measured by the wind LiDAR at height of 19 m (horizontal dashed lines indicate the 25th-75th percentile range of the entire time series). The selected high-/low-streamwise-velocity events are indicated with red and blue markers, respectively; (b, c) Contours of the uniform momentum zones extracted from the SLPIV streamwise velocity for the low- and high-streamwise-velocity events, respectively; (d, e) swirling strength, λ_{ci} overlapped with the quiver plot of the fluctuating velocity field for the low- and high-streamwise-velocity events, respectively. Local convection velocities of 7.1 m s^{-1} (d) and 6.7 m s^{-1} (e) were subtracted following Adrian et al. (2000a) (for clarity vectors were skipped). The thick arrows indicate the prevalent direction of sweeps, (Q_4), and ejection, (Q_2), turbulent events.

simulations, and near-ground smoke visualizations of the ASL (Wallace et al. 1972; Adrian et al. 2000b; Christensen and Adrian 2001; Hommema 2003; Morris et al. 2007).

The presence of negative vorticity along a shear layer is typically associated with the occurrence of turbulent ejections, which are denoted as Q_2 events, inducing local reduction of the streamwise velocity and upward vertical velocity fluctuations ($u' < 0, w' > 0$) (Wallace et al. 1972; Christensen and Adrian 2001; Adrian et al. 2000b; Morris et al. 2007).

A completely different scenario is observed for the selected large-scale high-streamwise-velocity event. The ISLs compress UMZs toward the ground while moving downstream (Fig. 9c), thus displaying an opposite inclination as compared to those observed for the low-streamwise-velocity event, and a different distribution of streamwise velocity fluctuation (Q_4 with $u' > 0, w' < 0$).

To further characterize interactions among turbulent structures with different scales, we analyze two variables describing the intensity of small-scale turbulence, namely swirling strength, λ_{ci} marking vortex cores, and TKE dissipation rate, ϵ (Albertson et al. 1997; Pope 2000; Christensen and Adrian 2001; Bodini et al. 2020; Sanchez Gomez et al. 2021). We calculate statistics of λ_{ci} and ϵ from the SLPIV data conditionally sampled through the value of the streamwise velocity calculated from the LiDAR fixed-point measurements at $z = 19$ m, $U_{LiD,z}$, which can significantly be affected by the energy carried by VLSMs and superstructures (Baars and Marusic 2020; Hu et al. 2020; Puccioni et al. 2023a). Specifically, the LiDAR streamwise velocity collected at a 19-m height, $U_{LiD,z}$, is binned as for the histogram reported in Fig. 10a with grey bars. Subsequently, statistics computed on the SLPIV and sonic-anemometer data are calculated within each bin identified through the simultaneous LiDAR velocity measurements. Assuming small-scale isotropy and using temporal derivatives of the velocity field, the TKE dissipation rate can be calculated as:

$$\epsilon_t(x,z,t) \approx 15\nu/\langle U(z)\rangle_x^2 (\partial u'(x,z,t)/\partial t)^2, \qquad (3)$$

where $\langle U(z)\rangle_x$ is the horizontally averaged streamwise velocity along the streamwise extent of the SLPIV field of view (Saddoughi and Veeravalli 1994). Furthermore, by leveraging 2D instantaneous spatial derivatives calculated from the highly spatially-resolved SLPIV snapshots, dissipation can also be computed following Doron et al. (2001); Wang et al. (2021), which is indicated through

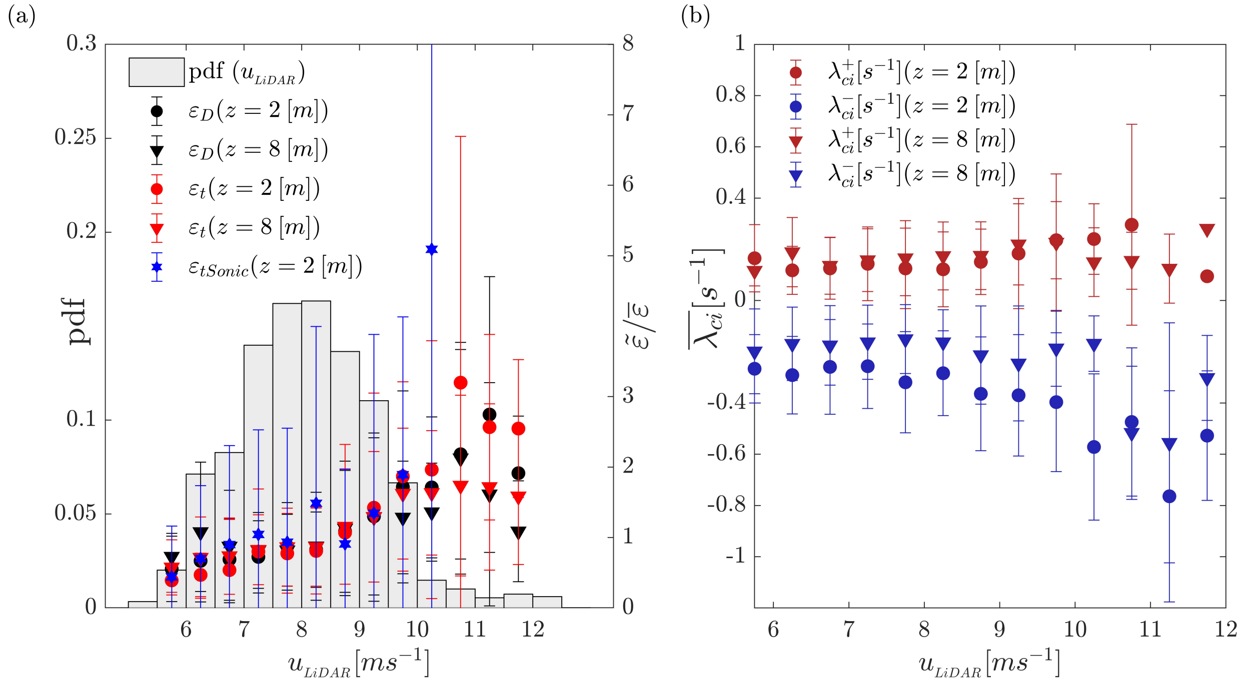

Fig. 10. Turbulence parameters calculated from data collected on February 22, 2022, through SLPIV at heights of 2 m, and 8 m, and a sonic anemometer, conditionally sampled based on the LiDAR data measured at z = 19 m, u_{LiDAR}: (a) TKE dissipation rate, $\tilde{\varepsilon}$ normalized by the spatially-averaged, height-dependent mean value $\overline{\varepsilon}$; The gray solid bars represent the histogram of u_{LiDAR}; (b) swirling strength λ_{ci} (red and blue markers, "+" and "−" superscripts, indicate positive and negative vorticity, respectively).

the parameter:

$$\varepsilon_D = 3\nu\left[\overline{\left(\frac{\partial u'}{\partial x}\right)^2} + \overline{\left(\frac{\partial w'}{\partial z}\right)^2} + \overline{\left(\frac{\partial u'}{\partial z}\right)^2} + \overline{\left(\frac{\partial w'}{\partial x}\right)^2} + 2\overline{\frac{\partial u'}{\partial z}\frac{\partial w'}{\partial x}} + 2/3\overline{\frac{\partial u'}{\partial x}\frac{\partial w'}{\partial z}}\right]. \quad (4)$$

The SLPIV data are then conditionally sampled for the various bins used in the histogram reported in Fig. 10a. The conditional statistic for the dissipation, calculated either through temporal or spatial derivative (ε_t and ε_D, respectively) are reported in Fig. 10a for the SLPIV data collected at heights of 2 m, 8 m, and from the sonic anemometer as well. Both methods used to estimate TKE dissipation rate generally show increased dissipation for larger values of u_{LiDAR}. This trend is amplified at the lower height of z = 2 m, for both spatial and temporal estimates, and for both SLPIV and sonic anemometer data. This analysis suggests that with increasing streamwise velocity aloft, thus with increasing wind shear, the spatio-temporal organization of the turbulent eddies located in the near-surface region leads to sharper velocity fluctuations, thus to enhanced dissipative processes draining energy from larger coherent structures toward smaller structures dominating viscous processes. While dissipative processes are known to be inherently related to the velocity derivative tensor and small-scale structures of turbulence (see, e.g., Chacin and Cantwell (2000)), probing the spatio-temporal variability of these processes in a high Reynolds-number boundary layer, such as the ASL, is a novel capability enabled by SLPIV.

A similar conditional statistical analysis is then performed for the vorticity field measured through the SLPIV, thus by analyzing the parameter $_{}$ The results reported in Fig. 10b show that the intensity of prograde (negative $_{}$) vortices increases with larger outer-scale velocity $_{},$ which is a direct consequence of the increased mean shear. This effect is remarkably evident close to the wall ($ = 2$ m) and for higher values of $_{}.$

c. Spatio-temporal coupling of SLPIV and LiDAR data

Leveraging the simultaneous availability of LiDAR fixed-point measurements covering the entire ASL height and high-resolution SLPIV measurements in the near-surface region, it is possible to retrieve compelling flow reconstructions over a streamwise–vertical plane as a function of time. The area covered for this analysis spans the vertical range from 1 m up to $O(10^2\,)$ height and for a streamwise extent of about 500 m. This analysis provides the opportunity to tackle important scientific questions on turbulence processes triggered by large-scale turbulent motions, which achieve their maximum energy typically at a height of about 20% of the ASL height (Hu et al. 2020; Puccioni et al. 2023a).

A crucial point for this analysis is the conversion of the time stamp of the LiDAR measurements in streamwise coordinate through Taylor's hypothesis of frozen turbulence (Taylor 1938). Specifically, a velocity time series is converted into a spatial record by leveraging the advection velocity of the flow, $_{\mathrm{adv}}$ (Taylor 1938; Del Álamo and Jiménez 2009; Moin 2009; Higgins et al. 2012; Han et al. 2019). If we assume all turbulent scales move with a constant speed at each given height, it is possible to apply the following time-to-space transformation (Zaman and Hussain 1981):

$$'(,,) = '(_0() - _{\mathrm{adv}}(),0), \tag{5}$$

where □$_0$(□) is the position of each LiDAR gate. It is typically a reasonable assumption to set □$_{\mathrm{adv}}$ equal to the local mean velocity □(□) (Taylor 1938).

An example of the coupling between the LiDAR and SLPIV data is provided for the February 22, 2022 data set in Fig. 11, which is extracted from video 2 provided in the Supplemental Material. The snapshots in Figs. 11a and 11c are extracted at the time 07:41:12 and 07:38:23 UTC, respectively. Notably, the advection velocity used to reconstruct the LiDAR streamwise coordinate is calculated at each time frame as a moving average over ±53 s for each height.

In Figs. 11a and c, the streamwise velocity calculated from the LiDAR fixed-point measurements and reconstructed in space is coupled with the respective SLPIV snapshot. Furthermore, the instantaneous velocity data recorded with the LiDAR fixed-point measurements are reported in

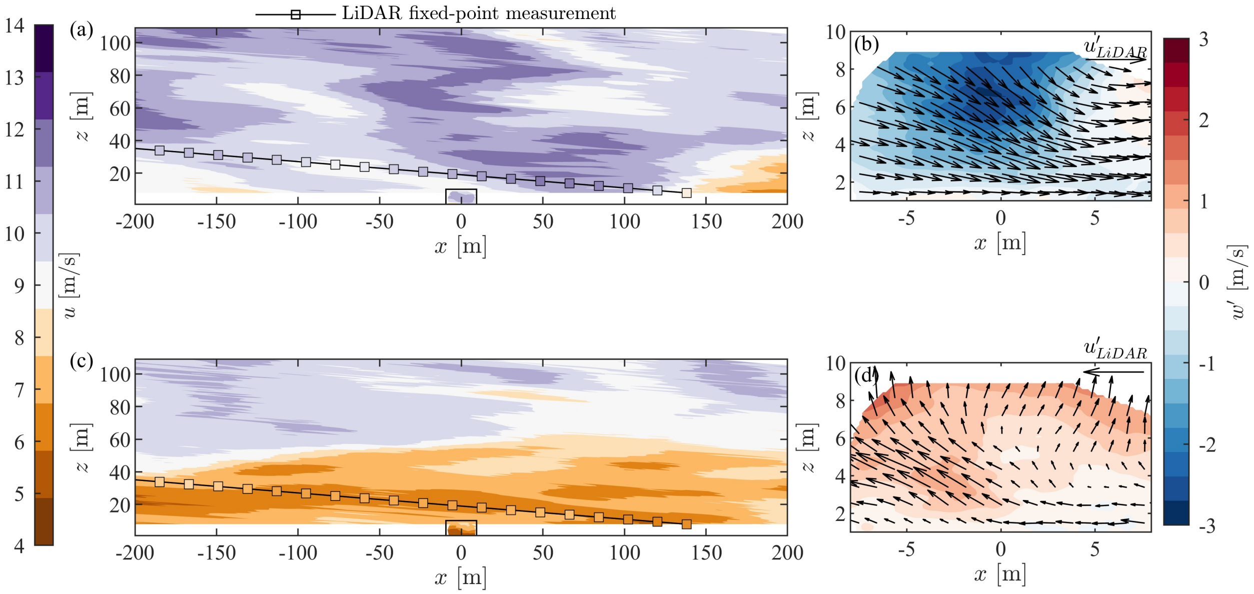

Fig. 11. Coupling SLPIV data and spatially-reconstructed LiDAR fixed-point measurements: (a; b) high streamwise-velocity event; (c; d) low streamwise-velocity event; (a; c) streamwise velocity calculated from the LiDAR fixed-point measurements and spatially transformed through Taylor's hypothesis of frozen turbulence coupled with the respective SLPIV snapshot (rectangle at the bottom center). Location and data of the LiDAR fixed-point measurements are reported with a line with square markers; (b; d) color map of SLPIV fluctuating vertical velocity overlapped with the quiver plot of the in-plane fluctuating velocity components. The arrow at the top-right corner corresponds to the fluctuating streamwise velocity measured by the LiDAR at 19-m height. The positive □-coordinate is consistent with the wind direction.

space with a line with square markers reporting the LiDAR data at their corresponding actual physical locations. Remarkably, both instruments capture similar values of the streamwise velocity, with the SLPIV exhibiting higher spatial resolution.

The snapshots reported in Fig. 11a and 11c correspond to high and low, respectively, streamwise-velocity events, i.e. with positive and negative fluctuating velocity measured through the LiDAR fixed-point measurements at a height of 19 m. The respective SLPIV frames are reported in Fig. 11b and 11d as quiver plots of the fluctuating in-plane velocity overlapped with the color map of the fluctuating vertical velocity. It is noticed that the high streamwise momentum detected by the LiDAR ($u'_{LiDAR} > 0$ in Fig. 11b) is concurrent with a general negative fluctuating vertical velocity ($w' < 0$) probed by the SLPIV, which corresponds to sweeping turbulent motions (Q_4 events) (Wallace et al. 1972). In contrast, a low streamwise momentum event detected by the LiDAR ($u'_{LiDAR} < 0$ in Fig. 11d) corresponds to generally positive vertical velocity fluctuations ($w' > 0$), which are associated with turbulent ejection motions (Q_2).

This preliminary analysis carried out by coupling SLPIV with fixed-point measurements performed with scanning Doppler LiDARs corroborates the research potential obtainable by merging the near-ground high spatio-temporal resolution of the SLPIV measurements with the long range of the LiDAR measurements covering the entire ASL to investigate interactions between large-scale turbulent eddies and near-wall turbulence. This innovative measurement approach will be instrumental in unveiling physical processes underpinning boundary layer dynamics, scalar transport, particle (snow) deposition, wind energy harvesting, and many other physical phenomena and engineering applications occurring in high Reynolds-number turbulent boundary layers.

6. Summary

In this paper, the setup and first deployments of the Grand-scale Atmospheric Imaging Apparatus (GAIA) have been described. The imaging system of snow particles provided by GAIA has been operated to perform super large particle image velocimetry (SLPIV) over a O(20 m × 20 m) field-of-view near the ground, while the UT Dallas mobile LiDAR station probed the streamwise velocity field with a composite of scans throughout the entire height of the atmospheric surface layer (ASL) and over a volume encompassing the SLPIV field-of-view. The overarching goal of this experimental apparatus is to probe the ASL velocity field with adequate and variable spatio-temporal resolution throughout the ASL height, namely with increasing resolution by approaching the ground where turbulent structures have wavelengths comparable to their distance from the ground, yet achieving heights in the proximity of the ASL top to probe the evolution of large energy-containing turbulent structures.

Several case studies have been presented to demonstrate the experimental capabilities provided by operating synergistically SLPIV and scanning Doppler LiDARs. An analysis has been performed in the time domain emphasizing how SLPIV and wind LiDARs can provide good resolution to probe effects of high- and low-streamwise-velocity events induced by very-large coherent turbulent structures on the near-ground turbulence. Our analysis has demonstrated how the availability of wind LiDAR data covering the ASL facilitates enhanced and integrated analyses of SLPIV data close to the ground. This is achieved by retrieving conditional statistics based on LiDAR data collected at higher altitudes that cannot be attained by the SLPIV, but where large turbulent structures are more energetic.

In this work, we have documented how SLPIV is a versatile measurement technique designed to probe flow fields by imaging tracer particles within the flow. Forthcoming improvements of the experimental setup along with innovative techniques for image post-processing (Liu and Shen 2008; Zhang et al. 2023) might enable SLPIV applications in other environments, such as urban flows and pollutant dispersion.

The data sets collected during the GAIA field campaign are publicly shareable to promote cutting-edge research on the organization and dynamics of multi-scale turbulent structures in the ASL. Advancements in these topics will enable the development of improved numerical models for simulating and predicting turbulent boundary layers.

APPENDIX A

SLPIV data processing

Wind velocity data from SLPIV are obtained by processing video files recorded for imaging the snow particles. Before PIV correlation, these videos are first down-sampled in time, mapped from pixels into physical dimensions, and then pre-processed to enhance signal intensity. Image down-sampling is needed as the cameras can only record at a few fixed rates (e.g., 30, 60, or 120 Hz), thus an optimal delay between frames could not be set during the image acquisition.

Instead, the maximum frame rate available is chosen, and then specific frames are extracted in post-processing to achieve the optimal particle image displacement. Too small displacements result in poor resolution of the vertical velocity component (much smaller than the streamwise velocity), while displacements too large result in loss of correlation.

Mapping the image into object space, needed to obtain velocity measurements in physical units, involves dewarping the image based on the variation of magnification throughout the field of view (Hong et al. 2014). Knowing the ground distance of the camera from the base of the light sheet, which is measured with a GPS, and the inclination angle of the camera, the physical distance between each pixel and the associated point on the planar light sheet can be determined. Combined with the focal length of the camera lens, this provides the magnification of each pixel used to dewarp the image and map it into physical dimensions.

The rectified images are further pre-processed to enhance the signal using time-averaged background subtraction, followed by two additional spatial filters (see Fig. A1). PIV cross-correlation is implemented to retrieve 2D velocity vectors using LaVision DaVis software with a multi-pass interrogation scheme. This scheme finishes with a correlation spot size of 32×32 pixels^2 or 64×64 pixels^2 for the vertical or horizontal, respectively, light-sheet cases. Final correlation passes use a normalized correlation function with zero padding. Initial post-processing removes spurious vectors with an iterative normalized median filter, after which 95% vector yield remains.

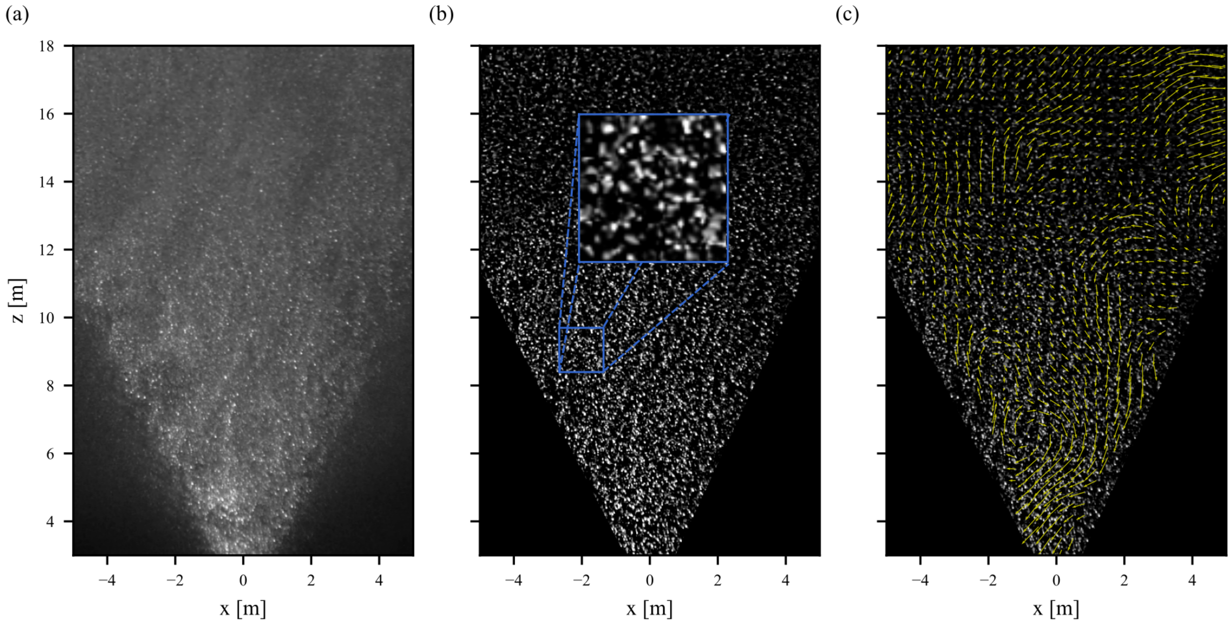

Fig. A1. Imaging of snow particles for SLPIV: (a) Raw image after rectification; (b) Enhanced image; (c) Raw image with fluctuating velocity vectors superimposed.

Acknowledgments. This research was mainly funded by the National Science Foundation, MRI program, Fluid Dynamics, Award No. 2018658. GVI, MP, SL, and CM are also funded by the National Science Foundation, Fluid Dynamics program, Award No. 1705837, and CAREER program, Award No. 2046160. The authors are thankful to Julie K. Lundquist for the fruitful discussions and the support in the preparation of the manuscript.

Data availability statement. The data presented in this paper are publicly shareable upon request to the PIs of the project J. Hong, M. Guala, and G.V. Iungo.

References

Abraham, A., and J. Hong, 2021: Operational-dependent wind turbine wake impact on surface momentum flux. *Renew. Sustain. Energ. Rev.*, **144**, 111 021, https://doi.org/https://doi.org/10.1016/j.rser.2021.111021.

Adrian, R., K. Christensen, and Z.-C. Liu, 2000a: Analysis and interpretation of instantaneous turbulent velocity fields. *Exp. Fluids*, **29 (3)**, 275–290, https://doi.org/https://doi.org/10.1007/s003489900087.

Adrian, R. J., C. D. Meinhart, and C. D. Tomkins, 2000b: Vortex organization in the outer region of the turbulent boundary layer. *J. Fluid Mech.*, **422**, 1–54, https://doi.org/https://doi.org/10.1017/S0022112000001580.

Albertson, J. D., M. B. Parlange, G. Kiely, and W. E. Eichinger, 1997: The average dissipation rate of turbulent kinetic energy in the neutral and unstable atmospheric surface layer. *J. Geoph. Res.: Atmos.*, **102 (D12)**, 13 423–13 432, https://doi.org/10.1029/96JD03346.

Baars, W., and I. Marusic, 2020: Data-driven decomposition of the streamwise turbulence kinetic energy in boundary layers. Part 1. Energy spectra. *J. Fluid Mech.*, **882**, A25, https://doi.org/10.1017/jfm.2019.834.

Balakumar, B., and R. Adrian, 2007: Large- and very-large-scale motions in channel and boundary-layer flows. *Philos. T. R. Soc. A.*, **365 (1852)**, 665–681, https://doi.org/10.1098/rsta.2006.1940.

Bartelt, P., and M. Lehning, 2002: A physical SNOWPACK model for the Swiss avalanche warning: Part I: numerical model. *Cold Regions Sci. Technol.*, **35 (3)**, 123–145, https://doi.org/ https://doi.org/10.1016/S0165-232X(02)00074-5.

Bodini, N., J. K. Lundquist, and M. Optis, 2020: Can machine learning improve the model representation of turbulent kinetic energy dissipation rate in the boundary layer for complex terrain? *Geosci. Model Develop.*, **13 (9)**, 4271–4285, https://doi.org/10.5194/gmd-13-4271-2020.

Bristow, N., J. Li, P. Hartford, M. Guala, and J. Hong, 2023: Imaging-based 3D particle tracking system for field characterization of particle dynamics in atmospheric flows. *Exp. Fluids*, **64 (78)**, s00 348–023–03 619–6, https://doi.org/https://doi.org/10.1007/s00348-023-03619-6.

Brugger, P., K. Träumner, and C. Jung, 2016: Evaluation of a procedure to correct spatial averaging in turbulence statistics from a Doppler lidar by comparing time series with an ultrasonic anemometer. *J. Atmos. Ocean. Technol.*, **33 (10)**, 2135–2144, https://doi.org/ 10.1175/JTECH-D-15-0136.1.

Brun, E., E. Martin, V. Simon, C. Gendre, and C. Coleou, 1989: An energy and mass model of snow cover suitable for operational avalanche forecasting. *J. Glaciology*, **35 (121)**, 333–342, https://doi.org/10.3189/S0022143000009254.

Calaf, M., M. Hultmark, H. J. Oldroyd, V. Simeonov, and M. B. Parlange, 2013: Coherent structures and the ⍰$^{-1}$ spectral behaviour. *Phys. Fluids*, **25 (12)**, https://doi.org/10.1063/1.4834436.

Cardesa, J. I., A. Vela-Martín, and J. Jiménez, 2017: The turbulent cascade in five dimensions. *Science*, **357 (6353)**, 782–784, https://doi.org/doi:10.1126/science.aan793.

Chacin, J. M., and B. J. Cantwell, 2000: Dynamics of a low Reynolds number turbulent boundary layer. *Journal of Fluid Mechanics*, **404**, 87–115, https://doi.org/https://doi.org/10.1017/ S002211209900720X.

Chamecki, M., C. Meneveau, and M. B. Parlange, 2009: Large eddy simulation of pollen transport in the atmospheric boundary layer. *J. Aerosol Scie.*, **40 (3)**, 241–255, https://doi.org/10.1016/j. jaerosci.2008.11.004.

Cheynet, E., J. B. Jakobsen, J. Snæbjörnsson, J. Mann, M. Courtney, G. Lea, and B. Svardal, 2017: Measurements of surface-layer turbulence in a wide Norwegian fjord using synchronized long-range Doppler wind LiDARs. *Remote Sensing*, **9 (10)**, 977, https://doi.org/https://doi.org/10.3390/rs9100977.

Christensen, K. T., and R. J. Adrian, 2001: Statistical evidence of hairpin vortex packets in wall turbulence. *J. Fluid Mech.*, **431**, 433–443, https://doi.org/10.1017/S0022112001003512.

Clauser, F. H., 1954: Turbulent boundary layers in adverse pressure gradients. *J. Aeron. Sci.*, **21 (2)**, 91–108, https://doi.org/https://doi.org/10.2514/8.2938.

Dasari, T., Y. Wu, Y. Liu, and J. Hong, 2019: Near-wake behaviour of a utility-scale wind turbine. *J. Fluid Mech.*, **859**, 204–246, https://doi.org/10.1017/jfm.2018.779.

de Silva, C. M., N. Hutchins, and I. Marusic, 2016: Uniform momentum zones in turbulent boundary layers. *Journal of Fluid Mechanics*, **786**, 309–331, https://doi.org/https://doi.org/10.1017/jfm.2015.672.

Del Álamo, J. C., and J. Jiménez, 2009: Estimation of turbulent convection velocities and corrections to Taylor's approximation. *J. Fluid Mech.*, **640**, 5–26, https://doi.org/https://doi.org/10.1017/S0022112009991029.

Dennis, D. J., and T. B. Nickels, 2008: On the limitations of Taylor's hypothesis in constructing long structures in a turbulent boundary layer. *J. Fluid Mech.*, **614**, 197–206, https://doi.org/https://doi.org/10.1017/S0022112008003352.

Doron, P., L. Bertuccioli, J. Katz, and T. Osborn, 2001: Turbulence characteristics and dissipation estimates in the coastal ocean bottom boundary layer from PIV data. *J. Phys. Ocean.*, **31**, 2108–2134, https://doi.org/https://doi.org/10.1175/1520-0485(2001)031<2108:TCADEI>2.0.CO;2.

Eaton, J., and J. Fessler, 1994: Preferential concentration of particles by turbulence. *Int. J. Multiph. Flow*, **20**, 169–209, https://doi.org/https://doi.org/10.1016/0301-9322(94)90072-8.

El-Asha, S., L. Zhan, and G. V. Iungo, 2017: Quantification of power losses due to wind turbine wake interactions through SCADA, meteorological and wind LiDAR data. *Wind Energy*, **20 (11)**, 1823–1839, https://doi.org/https://doi.org/10.1002/we.2123.

Erm, L., and P. Joubert, 1991: Low-Reynolds-number turbulent boundary layers. *J. Fluid Mech.*, **230**, 1–44, https://doi.org/https://doi.org/10.1017/S0022112091000691.

Frehlich, R., S. Hannon, and S. Henderson, 1998: Coherent Doppler lidar measurements of wind field statistics. *Bound.-Layer Meteorol.*, **86 (2)**, 233–256, https://doi.org/10.1023/A:1000676021745.

Fuertes, F. C., G. V. Iungo, and F. Porté-Agel, 2014: 3D turbulence measurements using three synchronous wind lidars: Validation against sonic anemometry. *J. Atmos. Ocean. Technol.*, **31 (7)**, 1549–1556, https://doi.org/https://doi.org/10.1175/JTECH-D-13-00206.1.

Ganapathisubramani, B., N. Hutchins, W. Hambleton, E. Longmire, and I. Marusic, 2005: Investigation of large-scale coherence in a turbulent boundary layer using two-point correlations. *J. Fluid Mech.*, **524**, 57–80, https://doi.org/10.1017/S0022112004002277.

Gromke, C., C. Manes, B. Walter, M. Lehning, and M. Guala, 2011: Aerodynamic roughness length of fresh snow. *Bound.-Layer Meteorol.*, **141 (1)**, 21–34, https://doi.org/DOI10.1007/s10546-011-9623-3.

Guala, M., S. Hommema, and R. Adrian, 2006: Large-scale and very-large-scale motions in turbulent pipe flow. *J. Fluid Mech.*, **554**, 521–542, https://doi.org/10.1017/S0022112006008871.

Guala, M., M. Metzger, and B. J. McKeon, 2010: Intermittency in the atmospheric surface layer: Unresolved or slowly varying? *Physica D: Nonlinear Phenom.*, **239 (14)**, 1251–1257, https://doi.org/https://doi.org/10.1016/j.physd.2009.10.010.

Guala, M., M. Metzger, and B. J. McKeon, 2011: Interactions within the turbulent boundary layer at high Reynolds number. *J. Fluid Mech.*, **666**, 573–604, https://doi.org/10.1017/S0022112010004544.

Han, G., G. Wang, and X. Zheng, 2019: Applicability of Taylor's hypothesis for estimating the mean streamwise length scale of large-scale structures in the near-neutral atmospheric surface layer. *Bound.-Layer Meteorol.*, **172 (2)**, 215–237, https://doi.org/10.1007/s10546-019-00446-3.

Heisel, M., T. Dasari, Y. Liu, J. Hong, F. Coletti, and M. Guala, 2018: The spatial structure of the logarithmic region in very-high-Re rough wall turbulent boundary layers. *J. Fluid Mech.*, **857**, 704–747, https://doi.org/10.1017/jfm.2018.759.

Heisel, M., C. M. de Silva, N. Hutchins, I. Marusic, and M. Guala, 2020: On the mixing length eddies and logarithmic mean velocity profile in wall turbulence. *J. Fluid Mech.*, **887**, R1, https://doi.org/10.1017/jfm.2020.23.

Heisel, M., C. M. de Silva, N. Hutchins, I. Marusic, and M. Guala, 2021: Prograde vortices, internal shear layers and the Taylor microscale in high-Reynolds-number turbulent boundary layers. *J. Fluid Mech.*, **920**, A52, https://doi.org/10.1017/jfm.2021.478.

Higgins, C. W., M. Froidevaux, V. Simeonov, N. Vercauteren, C. Barry, and M. B. Parlange, 2012: The effect of scale on the applicability of Taylor's frozen turbulence hypothesis in the atmospheric boundary layer. *Bound.-Layer Meteorol.*, **143 (2)**, 379–391, https://doi.org/DOI10.1007/s10546-012-9701-1.

Högström, U., 1990: Analysis of turbulence structure in the surface layer with a modified similarity formulation for near neutral conditions. *J. Atmos. Sci.*, **47 (16)**, 1949–1972, https://doi.org/10.1175/1520-0469(1990)047<1949:AOTSIT>2.0.CO;2.

Högström, U., 1992: Further evidence of “inactive" turbulence in the near neutral atmospheric surface layer. *Proceedings, 10th symposium of turbulence and diffusion*, Vol. 29, 188–191.

Högström, U., J. Hunt, and A.-S. Smedman, 2002: Theory and measurements for turbulence spectra and variances in the atmospheric neutral surface layer. *Bound.-Layer Meteorol.*, **103 (1)**, 101–124, https://doi.org/https://doi.org/10.1023/A:1014579828712.

Hommema, R. J., S. E. & Adrian, 2003: Packet structure of surface eddies in the atmospheric boundary layer. *Bound.-Layer Meteorol.*, **106 (1)**, 147–170, https://doi.org/https://doi.org/10.1023/A:1020868132429.

Hong, J., M. Toloui, L. P. Chamorro, M. Guala, K. B. Howard, S. Riley, J. Tucker, and F. Sotiropoulos, 2014: Natural snowfall reveals large-scale flow structures in the wake of a 2.5-MW wind turbine. *Nature Comm.*, **5**, 4216, https://doi.org/10.1038/ncomms5216.

Hu, R., X. I. Yang, and X. Zheng, 2020: Wall-attached and wall-detached eddies in wall-bounded turbulent flows. *J. Fluid Mech.*, **885**, https://doi.org/https://doi.org/10.1017/jfm.2019.980.

Huang, K., and Coauthors, 2021: Investigation of the atmospheric surface layer using a novel high-resolution sensor array. *Exp. Fluids*, **62 (4)**, 1–13, https://doi.org/10.1007/s00348-021-03173-z.

Hutchins, N., and I. Marusic, 2007a: Evidence of very long meandering features in the logarithmic region of turbulent boundary layers. *J. Fluid Mech.*, **579**, 1–28, https://doi.org/10.1017/S0022112006003946.

Hutchins, N., and I. Marusic, 2007b: Large-scale influences in near-wall turbulence. *Phil. Trans. Roy. Soc. A*, **365 (1852)**, 647–664, https://doi.org/https://doi.org/10.1098/rsta.2006.1942.

Hwang, J., and H. Sung, 2018: Wall-attached structures of velocity fluctuations in a turbulent boundary layer. *J. Fluid Mech.*, **856**, 958–983, https://doi.org/10.1017/jfm.2018.727.

Iungo, G., and F. Porté-Agel, 2013: Measurement procedures for characterization of wind turbine wakes with scanning Doppler wind LiDARs. *Advanc. Sci. Res.*, **10 (1)**, 71–75, https://doi.org/https://doi.org/10.5194/asr-10-71-2013.

Iungo, G. V., 2016: Experimental characterization of wind turbine wakes: Wind tunnel tests and wind lidar measurements. *J. Wind Eng. Industr. Aerodyn.*, **149**, 35–39, https://doi.org/https://doi.org/10.1016/j.jweia.2015.11.009.

Iungo, G. V., R. Maulik, S. A. Renganathan, and S. Letizia, 2022: Machine-learning identification of the variability of mean velocity and turbulence intensity for wakes generated by onshore wind turbines: Cluster analysis of wind lidar measurements. *J. Renew. Sustain. Energ.*, **14 (2)**, https://doi.org/https://doi.org/10.1063/5.0070094.

Iungo, G. V., and F. Porté-Agel, 2014: Volumetric lidar scanning of wind turbine wakes under convective and neutral atmospheric stability regimes. *J. Atmos. Ocean. Technol.*, **31 (10)**, 2035–2048, https://doi.org/https://doi.org/10.1175/JTECH-D-13-00252.1.

Iungo, G. V., Y. T. Wu, and F. Porté-Agel, 2013: Field measurements of wind turbine wakes with lidars. *J. Atmos. Ocean. Technol.*, **30 (2)**, 274–287, https://doi.org/10.1175/JTECH-D-12-00051.1.

Jeong, J., and F. Hussain, 1995: On the identification of a vortex. *J. Fluid Mech.*, **285**, 69–94, https://doi.org/doi:10.1017/S0022112095000462.

Jiménez, J., 2004: Turbulent flows over rough walls. *Annu. Rev. Fluid Mech.*, **36**, 173–196, https://doi.org/doi:10.1146/annurev.fluid.36.050802.122103.

Jiménez, J., 2012: Cascades in wall-bounded turbulence. *Annu. Rev. Fluid Mech.*, **44**, 27–45, https://doi.org/10.1146/annurev-fluid-120710-101039.

Jiménez, J., and R. Moser, 2007: What are we learning from simulating wall turbulence? *Philos. Trans. Roy. Soc. A.*, **365 (1852)**, 715–732, https://doi.org/https://doi.org/10.1098/rsta.2006.1943.

Jiménez, P. A., J. Dudhia, J. F. González-Rouco, J. Navarro, J. P. Montávez, and E. García-Bustamante, 2012: A revised scheme for the WRF surface layer formulation. *Month. Weath. Rev.*, **140 (3)**, 898–918.

Juliano, T. W., B. Kosović, P. A. Jiménez, M. Eghdami, S. E. Haupt, and A. Martilli, 2022: "gray zone" simulations using a three-dimensional planetary boundary layer parameterization in the weather research and forecasting model. *Month. Weath. Rev.*, **150 (7)**, 1585 – 1619, https://doi.org/10.1175/MWR-D-21-0164.1, URL https://journals.ametsoc.org/view/journals/mwre/150/7/MWR-D-21-0164.1.xml.

Kim, K. C., and R. J. Adrian, 1999: Very large-scale motion in the outer layer. *Phys. Fluids*, **11 (2)**, 417–422, https://doi.org/https://doi.org/10.1063/1.869889.

Krug, D., W. Baars, N. Hutchins, and I. Marusic, 2019: Vertical coherence of turbulence in the atmospheric surface layer: connecting the hypotheses of Townsend and Davenport. *Bound.-Layer Meteorol.*, **172 (2)**, 199–214, https://doi.org/10.1007/s10546-019-00445-4.

Kunkel, G., 2003: An experimental study of the high Reynolds number turbulent boundary layer. *PhD Thesis, The University of Minnesota*.

Kunkel, G. J., and I. Marusic, 2006: Study of the near-wall-turbulent region of the high-Reynolds-number boundary layer using an atmospheric flow. *J. Fluid Mech.*, **548**, 375–402, https://doi.org/https://doi.org/10.1017/S0022112005007780.

Lamer, K., E. P. Luke, Z. Mages, E. C. Leghart, Z. Zhu, B. P. Treserras, R. Rawat, and A. M. Vogelmann, 2022: The impact of heat and inflow wind variations on vertical transport around a supertall building–The One Vanderbilt field experiment. *Science of The Total Environment*, **851**, 157 834, https://doi.org/https://doi.org/10.1016/j.scitotenv.2022.157834.

Lane, S., J. F. Barlow, and C. R. Wood, 2013: An assessment of a three-beam Doppler lidar wind profiling method for use in urban areas. *J. Wind Eng. Industr. Aerodyn.*, **119**, 53–59, https://doi.org/https://doi.org/10.1016/j.jweia.2013.05.010.

Laskari, A., R. de Kat, R. J. Hearst, and B. Ganapathisubramani, 2018: Time evolution of uniform momentum zones in a turbulent boundary layer. *J. Fluid Mech.*, **842**, 554–590, https://doi.org/10.1017/jfm.2018.126.

Lee, M., and R. Moser, 2019: Spectral analysis of the budget equation in turbulent channel flows at high Reynolds number. *J. Fluid Mech.*, **860**, 886–938, https://doi.org/https://doi.org/10.1017/jfm.2018.903.

Lee, M., and R. D. Moser, 2015: Direct numerical simulation of turbulent channel flow up to ⍰ ⍰≈ 5200. *J. Fluid Mech.*, **774**, 395–415, https://doi.org/10.1017/jfm.2015.268, 1410.7809.

LeHew, J., M. Guala, and B. McKeon, 2011: A study of the three-dimensional spectral energy distribution in a zero pressure gradient turbulent boundary layer. *Exp Fluids*, **51 (1)**, 997–1012, https://doi.org/10.1007/s00348-011-1117-z.

Letizia, S., L. Zhan, and G. V. Iungo, 2021a: LiSBOA (LiDAR Statistical Barnes Objective Analysis) for optimal design of lidar scans and retrieval of wind statistics-Part 1: Theoretical framework. *Atmos. Meas. Tech.*, **14 (3)**, 2065–2093, https://doi.org/10.5194/amt-14-2065-2021, 2005.06078.

Letizia, S., L. Zhan, and G. V. Iungo, 2021b: LiSBOA (LiDAR Statistical Barnes Objective Analysis) for optimal design of lidar scans and retrieval of wind statistics-Part 2: Applications to lidar measurements of wind turbine wakes. *Atmos. Meas. Tech.*, **14 (3)**, 2095–2113, https://doi.org/10.5194/amt-14-2095-2021.

Liu, H. Y., G. Wang, and X. Zheng, 2019a: Amplitude modulation between multi-scale turbulent motions in high-Reynolds-number atmospheric surface layers. *J. Fluid Mech.*, **861**, 585–607, https://doi.org/10.1017/jfm.2018.906.

Liu, T., and L. Shen, 2008: Fluid flow and optical flow. *Journal of Fluid Mechanics*, **614**, 253–291, https://doi.org/https://doi.org/10.1017/S0022112008003273.

Liu, Z., J. F. Barlow, P.-W. Chan, J. C. H. Fung, Y. Li, C. Ren, H. W. L. Mak, and E. Ng, 2019b: A review of progress and applications of pulsed Doppler wind LiDARs. *Remote Sensing*, **11 (21)**, 2522, https://doi.org/https://doi.org/10.3390/rs11212522.

Mahrt, L., 1989: Intermittency of atmospheric turbulence. *J. Atmos. Sci.*, **46 (1)**, 79–95, https://doi.org/10.1175/1520-0469(1989)046<0079:IOAT>2.0.CO;2.

Marusic, I., and N. Hutchins, 2008: Study of the log-layer structure in wall turbulence over a very large range of Reynolds number. *Flow Turbul. Combust.*, **81 (1-2)**, 115–130, https://doi.org/10.1007/s10494-007-9116-0.

Marusic, I., B. McKeon, P. Monkewitz, H. Nagib, A. Smits, and K. Sreenivasan, 2010: Wall-bounded turbulent flows at high Reynolds numbers: recent advances and key issues. *Phys. Fluids*, **22 (6)**, 065 103, https://doi.org/https://doi.org/10.1063/1.3453711.

Marusic, I., and J. P. Monty, 2018: Attached Eddy Model of Wall Turbulence. *Annu. Rev. Fluid Mech.*, **51 (1)**, 49–74, https://doi.org/10.1146/annurev-fluid-010518-040427.

Marusic, I., A. Uddin, and A. Perry, 1997: Similarity law for the streamwise turbulence intensity in zero-pressure-gradient turbulent boundary layers. *Phys. Fluids*, **9 (12)**, 3718–3726, https://doi.org/10.1063/1.869509.

Mathis, R., N. Hutchins, and I. Marusic, 2009: Large-scale amplitude modulation of the small-scale structures in turbulent boundary layers. *J. Fluid Mech.*, **628**, 311–337, https://doi.org/https://doi.org/10.1017/S0022112009006946.

Meinhart, C. D., and R. J. Adrian, 1995: On the existence of uniform momentum zones in a turbulent boundary layer. *Phys. Fluids*, **7 (4)**, 694–696, https://doi.org/10.1063/1.868594.

Metzger, M., B. McKeon, and H. Holmes, 2007: The near-neutral atmospheric surface layer: turbulence and non-stationarity. *Phil. Trans. Roy. Soc. A*, **365 (1852)**, 859–876, https://doi.org/https://doi.org/10.1098/rsta.2006.1946.

Moin, P., 2009: Revisiting Taylor’s hypothesis. *J. Fluid Mech.*, **640**, 1–4, https://doi.org/https://doi.org/10.1017/S0022112009992126.

Monin, A., and A. Obukhov, 1954: Basic laws of turbulent mixing in the surface layer of the atmosphere. *Contrib. Geophys. Inst. Acad. Sci. USSR*, **24 (151)**, 163–187.

Monty, J., N. Hutchins, H. H. Ng, and I. Marusic, 2009: A comparison of turbulent pipe, channel and boundary layer flows. *J. Fluid Mech.*, **632**, 431–442, https://doi.org/10.1017/S0022112009007423.

Morris, S. C., S. R. Stolpa, P. E. Slaboch, and J. C. Klewicki, 2007: Near-surface particle image velocimetry measurements in a transitionally rough-wall atmospheric boundary layer. *J. Fluid Mech.*, **580**, 319–338, https://doi.org/10.1017/S0022112007005435.

Mouri, H., T. Morinaga, and S. Haginoya, 2019: Unlikely existence of $⍰^{-1}_{⍰}$ spectral law in wall turbulence: an observation of the atmospheric surface layer. *Phys. Fluids*, **31 (3)**, https://doi.org/10.1063/1.5063545, URL http://dx.doi.org/10.1063/1.5063545.

Muñoz-Esparza, D., B. Kosović, J. Mirocha, and J. van Beeck, 2014: Bridging the transition from mesoscale to microscale turbulence in numerical weather prediction models. *Bound.-Layer Meteorol.*, **153**, 409–440, https://doi.org/DOI10.1007/s10546-014-9956-9.

Nemes, A., T. Dasari, J. Hong, M. Guala, and F. Coletti, 2017: Snowflakes in the atmospheric surface layer: observation of particle-turbulence dynamics. *J. Fluid Mech.*, **814**, 592–613, https://doi.org/https://doi.org/10.1017/jfm.2017.13.

Önder, A., and J. Meyers, 2018: On the interaction of very-large-scale motions in a neutral atmospheric boundary layer with a row of wind turbines. *J. Fluid Mech.*, **841**, 1040–1072, https://doi.org/10.1017/jfm.2018.86.

Perry, A., S. Henbest, and M. Chong, 1986: A theoretical and experimental study of wall turbulence. *J. Fluid Mech.*, **165**, 163–199, https://doi.org/https://doi.org/10.1017/S002211208600304X.

Perry, A. E., and I. Marušić, 1995: A wall-wake model for the turbulence structure of boundary layers. Part 1. Extension of the attached eddy hypothesis. *J. Fluid Mech.*, **298**, 361–388, https://doi.org/https://doi.org/10.1017/S0022112095003351.

Pope, S. B., 2000: *Turbulent flows*. Cambridge University Press, https://doi.org/https://doi.org/10.1088/0957-0233/12/11/70.

Puccioni, M., M. Calaf, E. R. Pardyjak, S. Hoch, T. J. Morrison, A. Perelet, and G. V. Iungo, 2023a: Identification of the energy contributions associated with wall-attached eddies and very-large-scale motions in the near-neutral atmospheric surface layer through wind lidar measurements. *J. Fluid Mech.*, **955**, A39, https://doi.org/10.1017/jfm.2022.1080.

Puccioni, M., and G. V. Iungo, 2021: Spectral correction of turbulent energy damping on wind lidar measurements due to spatial averaging. *Atmos. Meas. Tech.*, **14 (2)**, 1457–1474, https://doi.org/https://doi.org/10.5194/amt-14-1457-2021.

Puccioni, M., C. Moss, and G. V. Iungo, 2023b: Coupling wind lidar fixed and volumetric scans for enhanced characterization of wind turbulence and flow three-dimensionality. *Wind Energy*, https://doi.org/https://doi.org/10.1002/we.2865.

Saddoughi, S. G., and S. V. Veeravalli, 1994: Local isotropy in turbulent boundary layers at high Reynolds number. *J. Fluid Mech.*, **268**, 333–372, https://doi.org/https://doi.org/10.1017/S0022112094001370.

Salesky, S., and W. Anderson, 2020: Coherent structures modulate atmospheric surface layer flux-gradient relationships. *Phys. Rev. Lett.*, **125 (12)**, 124 501, https://doi.org/10.1103/physrevlett.125.124501.

Sanchez Gomez, M., J. K. Lundquist, P. M. Klein, and T. M. Bell, 2021: Turbulence dissipation rate estimated from lidar observations during the lapse-rate field campaign. *Earth System Science Data*, **13 (7)**, 3539–3549, https://doi.org/10.5194/essd-13-3539-2021, URL https://essd.copernicus.org/articles/13/3539/2021/.

Smits, A., B. McKeon, and I. Marusic, 2011: High–Reynolds number wall turbulence. *Annu. Rev. Fluid Mech.*, **43 (43)**, 353–375, https://doi.org/10.1146/annurev-fluid-122109-160753.

Sofiev, M., P. Siljamo, H. Ranta, and A. Rantio-Lehtimäki, 2006: Towards numerical forecasting of long-range air transport of birch pollen: theoretical considerations and a feasibility study. *Internat. J. Biometeorol.*, **50**, 392–402, https://doi.org/https://doi.org/10.1007/s00484-006-0027-x.

Stull, R. B., 1988: *An introduction to boundary layer meteorology*, Vol. 13. Springer Science & Business Media.

Talluru, K., R. Baidya, N. Hutchins, and I. Marusic, 2014: Amplitude modulation of all three velocity components in turbulent boundary layers. *J. Fluid Mech.*, **746**, R1, https://doi.org/10.1017/jfm.2014.132.

Taylor, G. I., 1938: The spectrum of turbulence. *Proc. Roy. Soc. London*, **164 (919)**, 476–490, https://doi.org/https://doi.org/10.1098/rspa.1938.0032.

Toloui, M., S. Riley, J. Hong, K. Howard, L. Chamorro, M. Guala, and J. Tucker, 2014: Measurement of atmospheric boundary layer based on super-large-scale particle image velocimetry using natural snowfall. *Exp. Fluids*, **55**, 1–14, https://doi.org/DOI10.1007/s00348-014-1737-1.

Townsend, A., 1976: *The Structure of Turbulent Shear Flow*. 2nd ed., Cambridge University Press.

Veers, P., and Coauthors, 2022: Grand challenges: wind energy research needs for a global energy transition. *Wind Energy Science*, **7 (6)**, 2491–2496, https://doi.org/10.5194/wes-7-2491-2022, URL https://wes.copernicus.org/articles/7/2491/2022/.

Wallace, J. M., H. Eckelmann, and R. S. Brodkey, 1972: The wall region in turbulent shear flow. *J. Fluid Mech.*, **54 (1)**, 39–48, https://doi.org/https://doi.org/10.1017/S0022112072000515.

Wang, G., F. Yang, K. Wu, Y. Ma, C. Peng, T. Liu, and L.-P. Wang, 2021: Estimation of the dissipation rate of turbulent kinetic energy: A review. *Chem. Eng. Sci.*, **229**, 116 133, https://doi.org/https://doi.org/10.1016/j.ces.2020.116133.

Wyngaard, J., L. Peltier, and S. Khanna, 1998: LES in the surface layer: Surface fluxes, scaling, and SGS modeling. *J. Atmos. Sci.*, **55 (10)**, 1733–1754, https://doi.org/https://doi.org/10.1175/1520-0469(1998)055<1733:LITSLS>2.0.CO;2.

Zaman, K. B. M. Q., and A. K. M. F. Hussain, 1981: Taylor hypothesis and large-scale coherent structures. *J. Fluid Mech.*, **112**, 379–396, https://doi.org/https://doi.org/10.1017/S0022112081000463.

Zhan, L., S. Letizia, and G. V. Iungo, 2020: Lidar measurements for an onshore wind farm: Wake variability for different incoming wind speeds and atmospheric stability regimes. *Wind Energy*, **23 (3)**, 501–527, https://doi.org/https://doi.org/10.1002/we.2430.

Zhang, Z., J. Wang, H. Zhao, Z. Mu, and L. Chen, 2023: Applicability of deep learning optical flow estimation for PIV methods. *Flow Measurement and Instrumentation*, 102398, https://doi.org/ https://doi.org/10.1016/j.flowmeasinst.2023.102398.